Experimental and CFD analyses of pollutant dispersion around an isolated cylindrical building

Amani Amamou, Hammouda Mahjoub, Khaled Al-Farhany, Nejla Mahjoub Said, Hervé Bournot

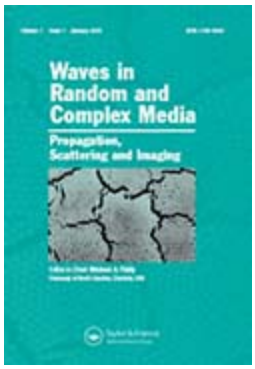

Experimental and CFD Analysis of Pollutant Dispersion around an Isolated Cylindrical Building

Journal:	*Waves in Random and Complex Media*
Manuscript ID	TWRM-2022-1707.R2
Manuscript Type:	Research Article
Date Submitted by the Author:	15-Jan-2023
Complete List of Authors:	amamou, amani; ENIM mahjoub, hammouda; ENIM Al-Farhany, Khaled; University of Al-Qadisiyah, Mechanical Engineering Dep. Said, Nejla Mahjoub; King Khalid University, Physic BOURNOT, Hervé ; Aix-Marseille Universite
Keywords:	experimental study, numerical simulation, pollutant dispersion, chimney, building, turbulent flow, Propagation, Imaging, Information transfer

Experimental and CFD Analysis of Pollutant Dispersion around an Isolated Cylindrical Building

Amani AMAMOU [1], Hammouda MAHJOUB [2], Khaled Al-FARHANY [3], Nejla MAHJOUB SAID [4, 5], Hervé BOURNOT [6]

[1] LGM, National Engineering School of Monastir, 5000 Monastir, University of Monastir, Tunisia

[2] LESTE, National Engineering School of Monastir, 5000 Monastir, University of Monastir, Tunisia

[3] Department of Mechanical Engineering, University of Al-Qadisiyah, Al-Qadisiyah, 58001, Iraq

[4] Department of Physics, College of Science, King Khalid University, Abha 61413, Saudi Arabia

[5] LGM, Preparatory Institute for Engineering Studies, University of Monastir, Tunisia

[6] Aix Marseille Univ, CNRS, IUSTI, Marseille, France

* Corresponding author E-mail : nalmahjoub@kku.edu.sa

Tel. +966543516940

ABSTRACT

An investigation of the dispersion of pollutants ejected from a chimney around a three-dimensional cylindrical obstacle within a crossflow air stream was conducted in this paper. The dynamic evolution of air seeded with glycerin particles ejected from an elevated jet around the isolated obstacle in a wind tunnel was experimentally studied using the Particle Image Velocimetry (PIV) technique and under different velocity ratios between the chimney ejection and the wind source. The dispersion of CO_2 pollutant around the cylindrical building was numerically predicted based on measured experimental data using the finite volume method and the Reynolds Stress Model. A good agreement between experimental and computational results was found. Velocity, temperature and concentration results revealed that the velocity of the wind together with the presence of the isolated building obstacle influenced the flow structure.

Keywords: experimental study; numerical simulation; turbulent flow; chimney; building; pollutant dispersion

Nomenclature

Symbol	Description	Unit
d	Chimney Diameter	m
D	Obstacle Diameter	m
h	Chimney height	m
H	Building Height	m
ℓ	wind tunnel height	m
F	Mass Fraction	
g	Gravitational Acceleration	m/s^2
G_k	Term of production due to buoyancy forces	$kg/(m\ s^3)$
Gr_d	Grashof number	
K	Kinetic Energy of Turbulence	m^2/s^2
P_k	Production term due to the mean gradients	$kg/(m\ s^3)$
R	Velocity Ratio	
Re	Reynolds number $\mathrm{Re} = \frac{v_0 d}{\upsilon}$	
S_{ij}	Mean Strain Rate	
T	Temperature	K
u_∞	Crossflow Velocity	m/s
v_0	Injection Velocity	m/s
$\overline{u_i'' u_j''}$	Reynolds stress	m^2/s^2
u_i, u_j	Velocity components along the i and j directions	
u, v, w	Velocity components along x, y, and z directions	m/s
x, y, z	Cartesian Coordinates	m
	Greek Symbols	
ρ	Density	Kg/m^3
β	Thermal Expansion Coefficient	K^{-1}
ε	Dissipation Rate of the Turbulent Kinetic energy	$m^2\ s^{-3}$
μ	Kinetic Viscosity	kg/(m s)
μ_t	Turbulent (or eddy) Viscosity	kg/(m s)
δ_{ij}	Kronecker symbol (=1 if i=j and 0 if i≠j)	
	Subscripts	
∞	Conditions in Crossflow	
0	Exit Section of the Jet	
	Superscripts	
$\bar{}$	Reynolds average	
$\tilde{}$	Favre average	

INTRODUCTION

The spread of a potentially dangerous contaminants ejected from a high point source, such as smokestack gases, is of significant interest due to their destructive effects on the safety and health of humans and the community. The buildings density and arrangement in the urban area influences the dispersion of emitted pollutants which prompted many researchers to investigate these complex phenomena both experimentally and numerically. Also, the presence of wind could be an important factor that affects the pollutant dispersion in urban environment. Numerous studies have been concentrated on the pollution diffusion under weak winds [1-3] and they showed that standard steady state Gaussian plume models generally overestimate pollutant concentrations at ground level under low wind conditions [4].

Several investigations have been performed to explore the flow behavior around an obstacle [5-7] using wind tunnel experiments. Higson et al. [8] conducted an experiment in the wind tunnel using a rotatable model building built on flat terrain. The wind tunnel experiments tend to over-estimate the situation with the highest concentrations found around the building and underestimate the situation when the pollutant concentrations were below or within the minimum range. This indicated that the continual changing direction of travel of the plume could have an effect on evaluation. Sada [9] simulated stack gas diffusion within an unstable atmospheric boundary layer over a coastal region using a wind tunnel experiment. The wind tunnel experimental results illustrated the maximum increase in pollutant concentration that could occur within a closer distance to the source when the level of convection was relatively stronger in atmosphere. Marvoidis et al. [10] conducted an experimental study of the dispersion of atmospheric pollutant around isolated obstacle of different shapes and orientation. They found that the presence of taller obstacle leads to a reduction of near ground concentrations. Dutta et al. [11] studied the flow structure past a square cylinder obstacle with different orientations and at two low Reynolds numbers (Re=97 and Re=187). The authors used two-component hot wire anemometry to measure the velocity. They concluded that dynamic features depend strongly on the cylinder orientation in the near wake however, in the far wake, this dependence becomes weak. Wind tunnel experiments have been conducted by Lin et al. [12] on high-buoyancy exhaust gas dispersion around an isolated cubic building under three exhaust speed ratios. Lin et al. [12] reported that the high buoyancy in diluting pollutant becomes more effective by increasing the exhaust ratio. Herein, they elucidated that high buoyancy and low exhaust ratio cause stronger concentration fluctuations.

Wind-tunnel tests represent a possible alternative to the field study which, despite the precision in following the dispersion of pollution in urban areas, costs much. In addition, generally it is not possible to determine

species concentration at different sensitive locations in a city owing to the significant cost and testing problems implied. Nevertheless, the necessity of understanding and predicting the pollutants dispersion properties under various conditions reinforces the use of computational fluid dynamics (CFD) approach. An experimental and numerical study of the flow around an isolated square cylinder has been conducted by Abdel dayem and Bayomi [13]. In this work, three Reynolds numbers were used (13.5×10^4, 9.5×10^4 and 6.8×10^4) and four angles of attack over the cylinder (0°, 15°, 30° and 45°) were tested. The process was repeated for the three considered Reynolds numbers. Four angles of attack of 0°, 15°, 30° and 45° were considered to study any possible flow direction around the cylinder. The authors turned to the CFD method, by the means of by the ANSYS code, to verify experimental data and to visualize the flow around the cylinder. A satisfactory agreement between computational and experimental results was found. Mahjoub et al. [14, 15] focused on the flowfield and turbulent structures behind an elevated jet by means of wind tunnel tests and computational simulations. They employed the particle image velocimetry (PIV) in measurements and retrieved experimental results were reported and validated with numerical calculations. Later, Mahjoub et al. [16] examined the flow behavior around single and double obstacles in a wind tunnel using a PIV technique and numerical simulations through the RSM turbulence model. The findings proved that the flow structures around the obstacles depend on the Reynolds number and the distance between the pair of obstacles. Based on their wind tunnel experiments [12], Lin et al. [17] reproduced the scenario of a high-buoyancy gas with one selected exhaust speed ratio to predict its dispersion around an isolated cubic building using the CFD software STAR-CCM+ 12.02.010. The target building model was set at a 1:50 scale and RANS and LES models have been assessed. The accuracy of the CFD models was validated in terms of velocity and concentration fields. The authors showed that both RANS and LES models correctly predict the concentration field, except that the RANS model overestimates the time-averaged concentration near the source. In the same context, the performance of RANS and LES models has been assessed by Ma et al. [18] through a confrontation between predicted and wind-tunnel experimental results. Likewise, the authors found that the LES model predicts better the time-averaged concentration field. Ma et al. [18] studied the influence of plume buoyancies on the dispersion of pollutants around a cubic building. They reported that the positive plume buoyancy increases the fluctuating concentration behind the obstacle, while the negative buoyancy limits the pollutants dilution in the wake region. Another parameter which influenced on the dispersion of pollutant around an isolated obstacle was the side ratio effect (building length- to-building width), as considered by Jiang and Yoshie [19]. In their study, Jiang and Yoshie performed numerical simulations using

LES model to analyze the effect of four different side ratios (from 0.25 to 1.5) on the gas dispersion around an isolated obstacle at a Reynolds number of Re=7500. Also, the authors have been strengthened their research by setting different source positions on the ground. For all treated cases, the main observation was the existence of a primary separation region at the ground level together with a recirculation region behind the high-rise building.

A variety of numerical studies has been conducted to investigate the flow and the dispersion of pollution from a pollutant elevated source whether in presence of an obstacle or not. Adair [20] investigated the three-dimensional dispersion of a non-floating passive scalar ejected from a chimney into a turbulent boundary layer. The author used a Reynolds-averaged Navier-Stokes method to solve the problem. Overall, a good agreement between predicted and measured concentrations has been obtained, expect in the far wake with the presence of a building. Wang and liang [21] examined the evolution of the flow over a three-dimensional obstacle. They studied the effect of the incidence angle. Huang et al. [22] examined the influence of roof edges on the wind velocity and the pollution distribution in an urban road using a two-dimensional model under the FLUENT code. The simulated dynamic and scalar fields showed clearly that the in-canyon vortex dynamics and the distribution of pollutants depend on the wedge-shaped roof configurations. The authors adopted the standard k-ε turbulence model in simulations. The same approach has been followed by Huang and Zhou [23] and Huang et al. [24] who investigated a two-dimensional computational model simulating the airflow and the dispersion of pollutants in urban street canyon with an elevated expressway [23] and taking into account different shapes and different heights of building roofs [24]. Huang et al. [25] treated numerically the ventilation problem of a large space mechanical plant with multiple pollution sources. The finite-volume based commercial software STAR-CD has been used for the calculation. The results of this CFD analysis showed the possibility of improvement of the pollution properties through the decrease of the buildings densities on the windward side and the reduction of obstacles in the perpendicular wind direction. Abassi et al. [26] used the Lattice Boltzmann equation with the BGK model to simulate a laminar flow around a square obstacle. The model has been validated by a comparison with experimental data obtained by PIV technique. The findings of large-scale simulated atmospheric flows stably stratified surrounding a large individual and complex shaped building are reported by Korycki et al. [27]. The authors revealed that the Froude number seems to be the major parameter that controlled the wake structures and vortex patterns. Keshavarzian et al. [28] have developed a numerical model to perform wind-flow and pollutant dispersal

simulations in the vicinity of a high-rise building. The effect of the location of the pollution source on the dispersion of the pollutant towards a building was studied.

As shown in the above literature review, many parameters could influence the flow structure surrounding an obstacle. In this paper, wind tunnel experiments on the dispersion of pollutants around an isolated cylindrical building have been conducted to evaluate the CFD simulations accuracy later. The evolution of the airflow and the pollutant dispersion has been represented by mean flow velocity vectors and associated turbulence parameters using the PIV technique and under different velocity ratios between the chimney ejection and the wind source. Afterwards, three-dimensional numerical simulations have been carried out to reproduce the same experimentally treated cases. The Navier-Stokes equations have been solved using the second-order turbulence RSM model. The comparison between the experimental data and predicted results showed a good agreement. The current computation method is intended to be applied to atmospheric dispersion. A practical case study illustrating the dispersion of CO_2 pollutant has been presented in terms of velocity, temperature and concentration fields.

EXPERIMENTAL SET-UP

In experiments, the chimney was emitting within a wind tunnel with a cross section of 0.2 m wide × 0.3 m high and 3 m long. The arrangement of the studied model is shown in Figure 1. The isolated cylinder obstacle and the air chimney were installed at the center plane far from the tunnel entrance. The wind tunnel was designed with a wooden and plastic-covered floor for visualization purposes, one side face made of wood and painted black to diminish light reflections, the other face made with Pyrex to provide optical access and the upper wall of the tunnel was open. The wind flow was coming from two sections at the entrance of the tunnel; the inferior one allowed velocities between 0 and 16 m/s while the superior entry section introduced velocities between 0 and 42 m/s. For present experiments, the velocity did not exceed 16 m/s, thus both lower and upper entrance sections were considered.

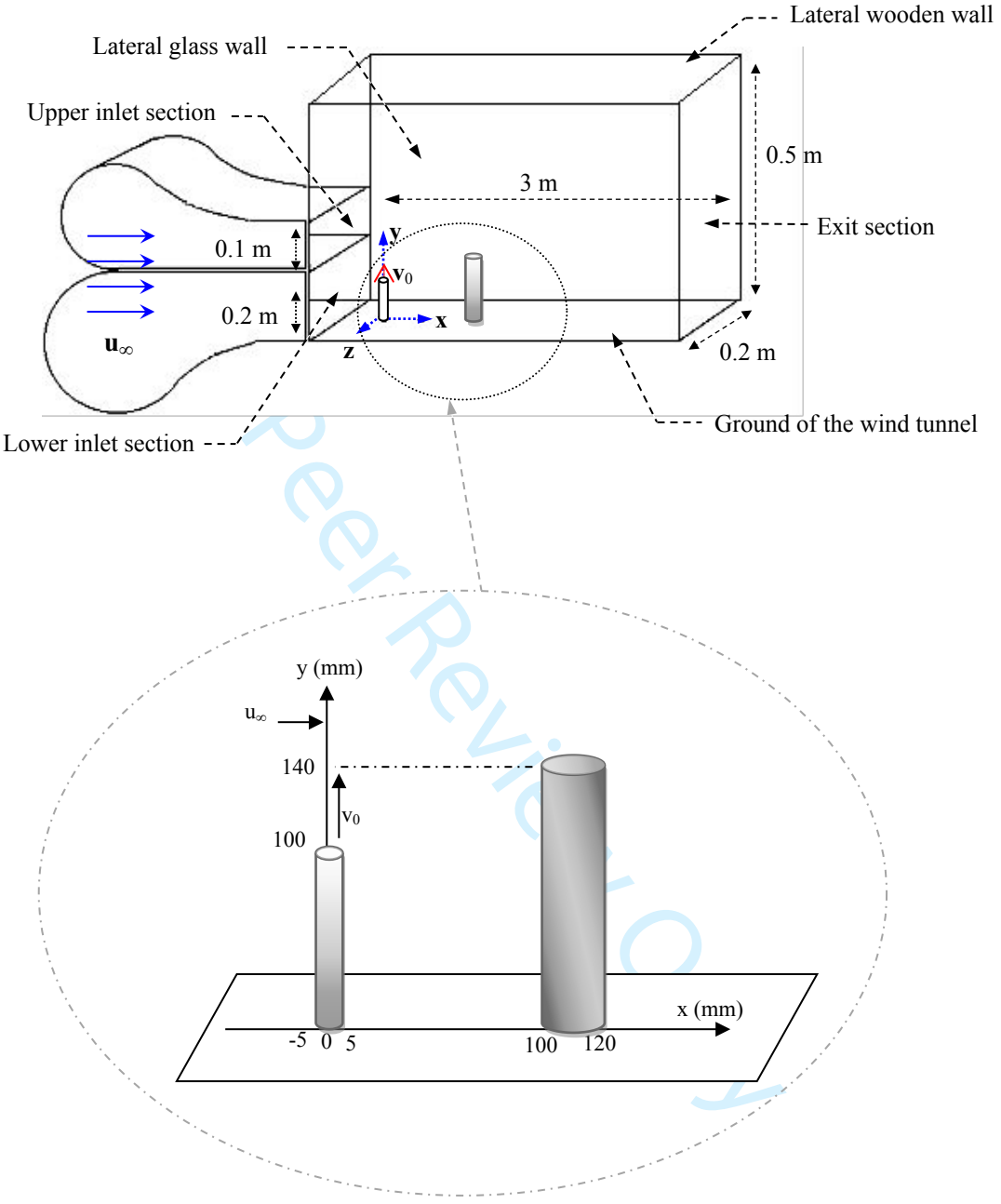

Figure 1. Chimney and obstacle positions in the wind tunnel

Several hot wire velocity measurements were carried out at the entrance of the wind tunnel. We consequently performed an accurate location of the Reynolds independent zone and justified the above mentioned 20-diameter emplacement of the chimney jet downstream of the wind tunnel inlet section. The efficiency of this set-up is further proved by Figure 2 where we represented the mainstream velocity revealing a shear layer width that did not exceed 10 mm and a global turbulence intensity level lower than 0.2%. Herein, we remind that the boundary layer thickness is defined as the point where the local velocity attains 99% of the free-stream velocity (the measurements are done without the chimney and the obstacle).

To show that the limits of the wind tunnel don't influence on the evolution of our problem, in Figure 3, we have observed the plume behavior in a horizontal plane, passing through the chimney exit section (xz plane). This visualization shows us shape factor, momentum thickness, displacement thickness. Indeed, we can observe vortex structures that show that the velocities along the z component, perpendicular to the plane (x, y) are not zero. When the wind tunnel flow is faster than the plume flow (figure 3.b), we can consider that the plume does not have its own motion: it follows the transverse flow in the wake that it creates after the chimney. We can see that the shape of the plume is analogous to the shape of a wake behind a cylinder. This shape is preserved when the velocity of the cross flow is lower (figure 3.a).

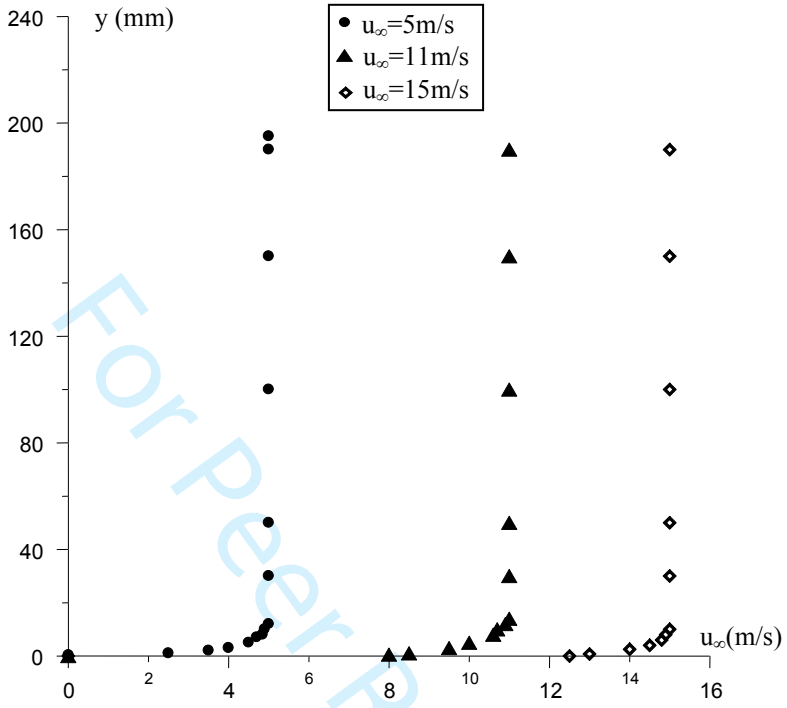

Figure 2. Mainstream velocity 20 diameters downstream of the inlet test cross section.

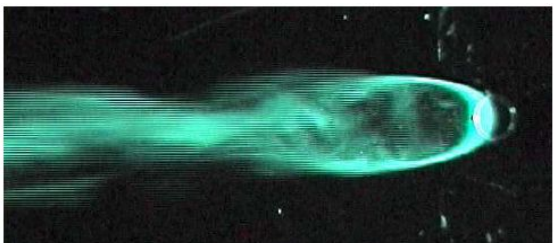

(a) Re= 5000, Re_ℓ= 1.5 10^5

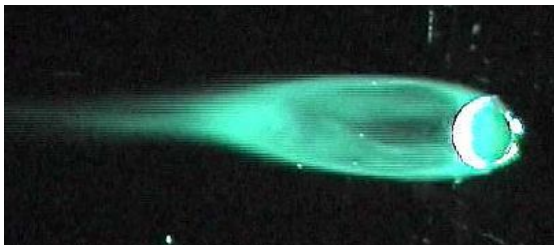

(b) Re= 5000, Re_ℓ= 2.25 10^5

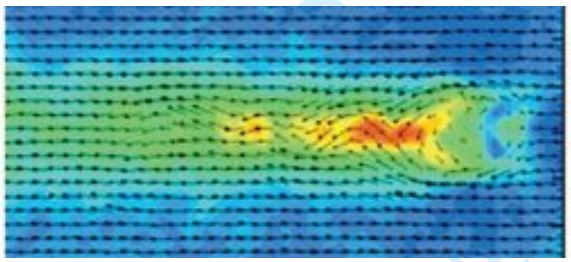

(c) PIV turbulence intensity

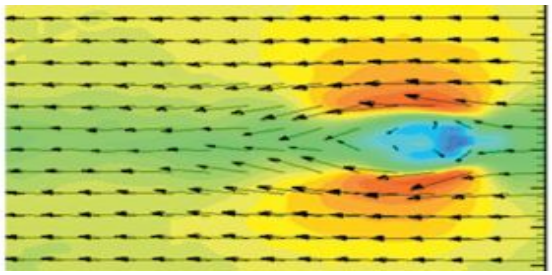

(d) PIV horseshoes vortices (velocity magnitude)

Figure 3. Different types of vortical structure associated with the chimney -jet near field in a horizontal plane y/d=1.1, without cylindrical obstacle

The air stream from the chimney was seeded with glycerin particles to identify its proper development. The density and the viscosity of the glycerin particle were $\rho = 1.23$ g/cm^3 and $\mu = 1.48\ 10^{-3}$ Pa.S, respectively, with a surface tension of $59.4\ 10^{-3}$ N/m and Refractive index 1.47. The particle diameter was approximately 1 µm. One milliliter of pure jet fluid contains an average density of 30 glycerin particles. The height and the diameter of the cylindrical obstacle were 140mm and 20mm, respectively.

The particle image velocimetry (PIV) technique was used to measure the instantaneous and mean dynamic fields and the hot wire anemometry technique was applied to determine the cross-flow velocity. The two-dimensional measurements using the PIV technique based on a TSI PowerView system [18] was then developed. This measurement technique needed a 50 mJ dual YAG laser generating two flat pulses with a single period of time between 5×10^{-9} and 10^{-8} s. It also required a high-resolution PowerView 4M cross-correlation camera to acquire the data images and a synchronizer. The windows software "Insight" was used for the acquisition, the processing and post-processing of the collected data. "Insight" permitted the synchronization of the pulses according to the observed phenomena, and the adjustment of the time step between two images. This time step was 70 µs. In order to avoid sub-pixel bias errors and spurious vectors, the velocity vectors were calibrated at 130 µmpixel^{-1} and limited to the representation of the velocity field in regions where the luminance was sufficiently strong. The average of the final fields is done over 500 successive acquisitions. ~~For each point, the experimental uncertainties were estimated as follows:~~ $\frac{V_{max} - V_{min}}{V_{av}}$ ~~where V_{max}, V_{min} and V_{av} are the maximum, the minimum and the average velocities measured, respectively. For these experiments, the uncertainties did not exceed 5%.~~ From the top of the wind tunnel, the sheet of light was directed by a 45° mirror giving rise to a shadow zone upstream of the obstacle where the measurements were not possible in this region.

The uncertainty of the experimental measurement has been quantified and calculated based on the works of Gomit et al. [29], Sciacchitano [30], as well as the GUM guide [31]. From the mathematical model $\left(Y = f(p_1, p_2, ..., p_n)\right)$ and the standard uncertainties *Un* of each parameter p_i, the combined uncertainty Un_c is estimated from the propagation law expressed in the form: $Un_c(Y)^2 = \sum_i^n (C_i)^2 \times Un(p_i)^2$ when the input quantities are independent. Herein, $C_i = \frac{\partial f}{\partial x_i}$ are the sensitivity coefficients. The expanded uncertainty is obtained by multiplying the compound uncertainty by a coverage factor *k*. In practice, a value of k equals to 2 is

often used. In the case of a normal distribution, this corresponds to a probability of 95% that the true value of the measured lies within the confidence interval.

As proposed by Gomit et al. [29], the two major contributions to PIV measurement uncertainties are the uncertainty related to the estimation of the magnification factor (calibration) and that related to the estimation of the displacement of the particles inside each interrogation cell.

In the experiments, a particular effort has been made on the calibration by adjusting the perpendicularity of the camera with the wall of the wind tunnel and the parallelism between the laser sheet to the wall. The uncertainty on the angle camera laser sheet was estimated less than 1 degree, which leads to an uncertainty on the flow velocity of about 10^{-3} m/s. The measurement of the 8 cm calibration ruler is assumed to be valid to within 2 px.

The uncertainty on the displacement of the particles estimated by the PIV algorithm is typically given in the literature as less than 0.1 pixel [32]. The TSI-Insight PIV algorithm has been tested [33] and gave better results compared to competitors, and we can reasonably take the value 0.05 pixel.

The particle size of the order of a micron is optimal [30] in this configuration for a good signal-to-noise ratio while ensuring a minimum slip velocity, calculated by means of Stokes' law in our case at 4 µm/s.

The synchronization of ND:Yag lasers is the one with the lowest systematic error [34] it can largely be considered negligible, especially in view of the flow velocities studied here.

All these values and their impact on the uncertainty of the total measured velocity are calculated and summarized in the table below for a measured velocity of 11 m/s.

Table 1. Experimental measurement uncertainty

p_i	$Un(p_i)$	$\lvert C_i \rvert . Un(p_i)$
Ruler length uncertainty (m)	7.22×10^{-5} m	1.10×10^{-2} m/s
Deplacement error	0.05 px	6.43×10^{-2} m/s
Pixel calibration error	2 px	2.6×10^{-2} m/s
Camera angle error	7.51×10^{-8} m	1.07×10^{-3} m/s
Slip velocity	4 µm/s	5.14×10^{-5} m/s
Combined uncertainty		0.07 m/s

From the standard uncertainty of each parameter, the combined uncertainty is then estimated from the law of propagation stated above as follows:

$$Un_c(V) = \sqrt{\sum_i^n (C_i)^2 \times (Un(p_i)^2} = 0.070\, m/s$$

The extended uncertainty is obtained by a coverage factor k=2, and the final measurement's result at the considered point is therefore: $V = 11.0 \pm 0.140\, m/s$ (k=2). The estimated uncertainty here is about 1.27% of the measured value.

Before setting the cylindrical obstacle, we intended to present the sectional instantaneous views of chimney - jet wakes evolutions for six different instances in Figure 4. The wake vortices are perhaps the most intriguing structures in the near field. They have some characteristics which are similar to wake vortices of solid cylinders, but differences between the chimney-jet (a fluid) and the cylinder (a solid) as obstacles to the crossflow suggest significant differences in how the wake vortices should form. Furthermore, if the "wake" is defined as the region downstream of the chimney-jet, between the jet and the chimney, it can immediately be seen that this is fundamentally different from a cylindrical obstacle - wake. Downstream of the chimney-jet, there appears to be a quiescent region with low vorticity (shown in blue). Further downstream, the flow contains larger scale features which move slowly in the direction of the crossflow.

Instantaneous realizations of the jet velocity field are very different from the corresponding ensemble-averaged fields. Figure 5 shows typical mean and instantaneous side-view images through the y/d=11 plane of a Re=1875. In this figure, the velocity vectors and the vorticity pattern on the horizontal plane (y/d=11) are shown. A recirculation zone is found in the jet-wake between the forward and aft stagnation points which are located on the symmetry axis z/d=0. Inside the recirculation zone, along the symmetry axis, reverse flows evolve from the aft stagnation point and go towards the forward stagnation point. The chimney jet generates vorticity for its own wake, of one sign on one side and of opposite sign on the other side. On the whole, the Karman vortex gradually grows up in the shear layer and moves towards the wake centerline. Just after passing through the wake bubble, it starts to move fast. As it goes downstream, it gets away from the centerline slightly and then turns to the centerline again. Finally, it moves parallel to the x axis. The paths of vortices shed at upper and lower sides meet together at the reattachment point. Far downstream, the lock-on makes the vortex remain much closer to the centerline. Thus, it appears that the upper and lower vortex streets are formed into a line.

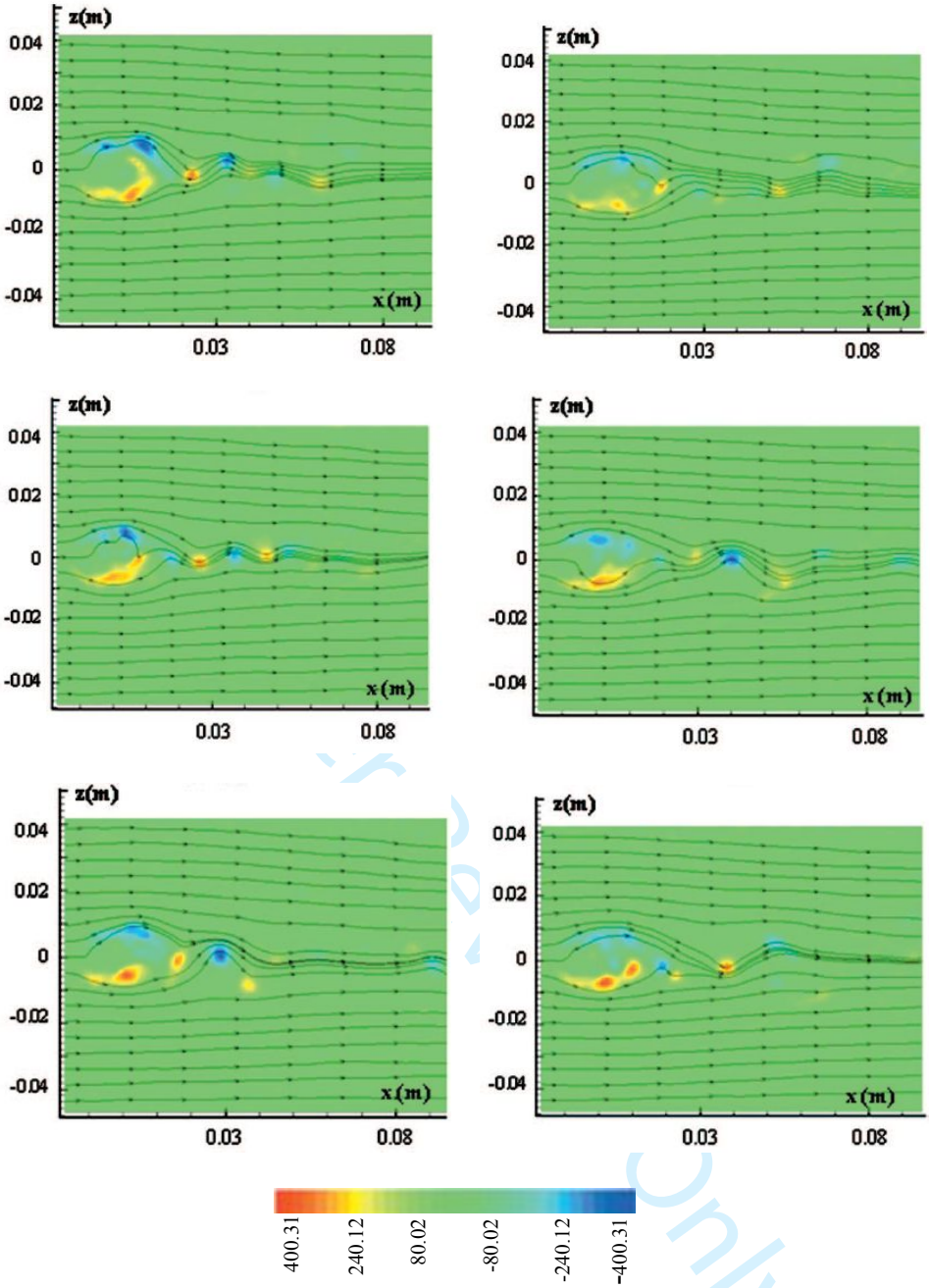

Figure 4. Cross-sectional instantaneous vorticities of the flow downstream chimney-jet and their wakes, Re=1875 and Re_ℓ=1.87 10^4

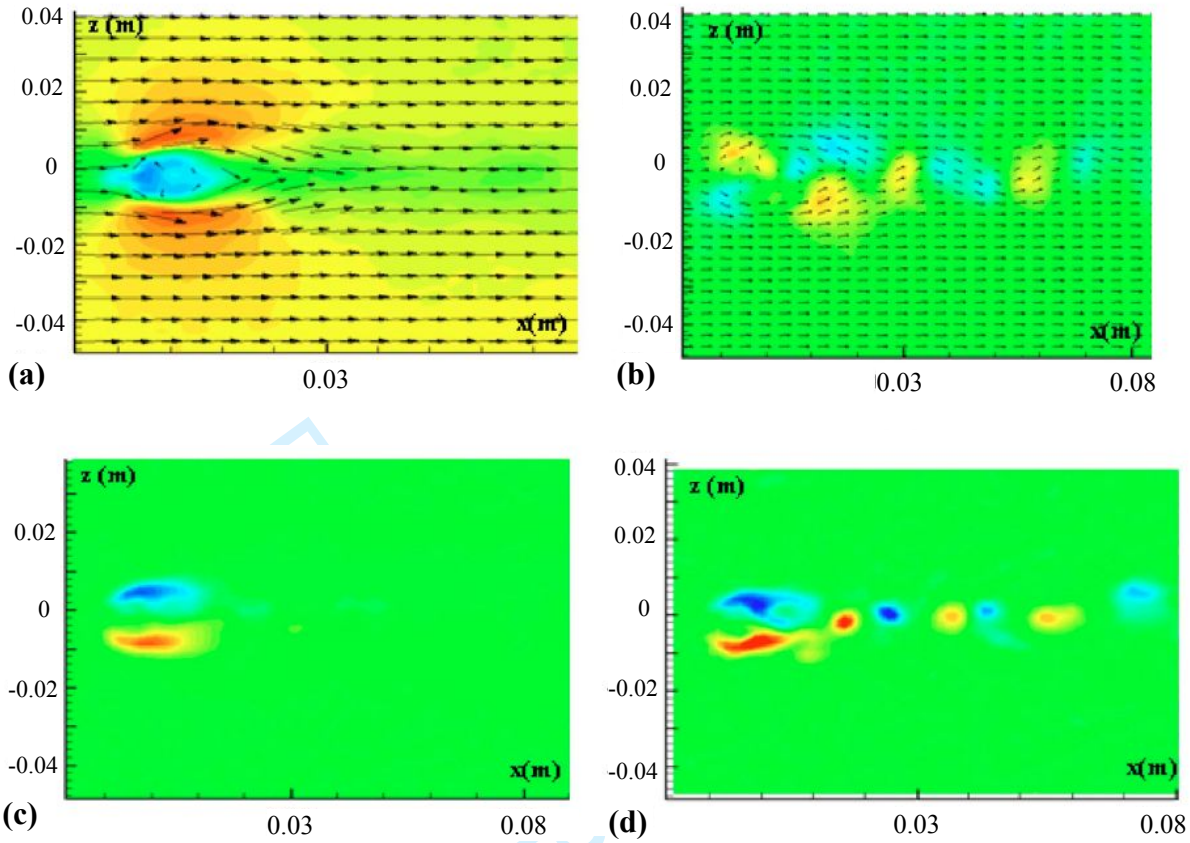

Figure 5. (a) Mean velocity field, (b) instantaneous longitudinal-velocity, (c) mean vorticity field, (d) instantaneous vorticity, Re=1875 and Re_t=1.87 10^4

COMPUTATIONAL SET-UP

The average of flow field around the chimney and the obstacle was obtained by changing the velocity of the crossfow stream u_∞. The flow was three-dimensional, turbulent and steady. The numerical approach used in this work was close to the one developed by Mahjoub et al. [35]. The conservation laws of mass, moment and energy were written by Navier's equations. The origin of this system corresponded to the center of the chimney based at the wind tunnel floor, as illustrated in Figure 1, with 'x' in the longitudinal direction, 'y' in the normal direction and 'z' in the lateral direction. The processed equations dealing with this problem were acquired through Favre decomposition and are expressed as follows:

Continuity equation:

$$\frac{\partial\left(\overline{\rho}\,\widetilde{u}_i\right)}{\partial x_i}=0 \tag{1}$$

Momentum equation:

$$\frac{\partial\left(\overline{\rho}\,\widetilde{u}_j\,\widetilde{u}_i\right)}{\partial x_j}=-\frac{\partial\,\overline{p}}{\partial x_i}+\frac{\partial}{\partial x_j}\left(\mu\frac{\partial\,\widetilde{u}_i}{\partial x_j}-\overline{\rho u_i'' u_j''}\right)+\left(\overline{\rho}_\infty-\overline{\rho}\right)g\,\delta_{ij} \tag{2}$$

Energy equation:

$$\frac{\partial\left(\overline{\rho}\,\widetilde{u}_j\,\widetilde{T}\right)}{\partial x_j}=\frac{\partial}{\partial x_j}\left(\frac{\mu}{Pr}+\frac{\mu_t}{\sigma_t}\right)\frac{\partial\,\widetilde{T}}{\partial x_j} \tag{3}$$

Mass fraction equation:

$$\frac{\partial\left(\overline{\rho}\,\widetilde{u}_j\,\widetilde{f}\right)}{\partial x_j}=\frac{\partial}{\partial x_j}\left(\frac{\mu}{Sc}+\frac{\mu_t}{\sigma_f}\right)\frac{\partial\,\widetilde{f}}{\partial x_j} \tag{4}$$

The above system of equations introduced an additional number of unknown parameters whose resolution required a closure turbulence model.

The second-order turbulence model; the Reynolds Stress Model (RSM), was selected in this numerical study based on previous findings of Mahjoub et al. [14, 35]. These authors pointed out that the RSM predicted the jet evolution in the exit region and in the leakage area better than first-order models. The RSM representative equation was given below:

$$\underbrace{\frac{\partial}{\partial x_k}\left(\overline{\rho}\,\widetilde{u}_k\,\overline{u_i'' u_j''}\right)}_{C_{ij}}=\underbrace{\frac{\partial}{\partial x_k}\mu\frac{\partial}{\partial x_k}\left(\overline{u_i'' u_j''}\right)}_{D_{ij}^{L}}\underbrace{-\overline{\rho}\left[\overline{u_i'' u_k''}\frac{\partial\,\widetilde{u}_j}{\partial x_k}+\overline{u_j'' u_k''}\frac{\partial\,\widetilde{u}_i}{\partial x_k}\right]}_{P_{ij}}+D_{ij}^{T}+G_{ij}+\phi_{ij}+\varepsilon_{ij} \tag{5}$$

With

C_{ij} : convective term.

D_{ij}^{L} : molecular diffusion

P_{ij} : stress production

D_{ij}^{T} : turbulent diffusion

G_{ij} : buoyancy production

ϕ_{ij} : pressure strain

ε_{ij} : dissipation rate of the turbulent kinetic energy

The equation expressing the kinetic turbulent energy (k) and the dissipation rate of the kinetic energy (ε) related to the RSM are given below:

$$\frac{\partial\left(\bar{\rho}\,\tilde{u}_j\,k\right)}{\partial x_j}=\frac{\partial}{\partial x_j}\left(\frac{\left(\mu+\mu_t\right)}{\sigma_k}\frac{\partial k}{\partial x_j}\right)+\frac{1}{2}\left(P_{ii}+G_{ii}\right)-\bar{\rho}\,\varepsilon \tag{6}$$

$$\frac{\partial\left(\bar{\rho}\,\tilde{u}_j\,\varepsilon\right)}{\partial x_j}=\frac{\partial}{\partial x_j}\left[\left(\mu+\frac{\mu_t}{\sigma_\varepsilon}\right)\frac{\partial \varepsilon}{\partial x_j}\right]+C_{\varepsilon 1}\frac{1}{2}\left(P_{ii}+C_{\varepsilon 3}G_{ii}\right)\frac{\varepsilon}{k}-C_{\varepsilon 2}\,\bar{\rho}\,\frac{\varepsilon^2}{k} \tag{7}$$

And: $P_{ii}=2\,\mu_t\left(\frac{\partial \tilde{u}_i}{\partial x_i}\right)^2$, $G_{ii}=2\,\beta\,g_i\,\frac{\mu_t}{\sigma_t}\frac{\partial \tilde{T}}{\partial x_i}$

The employed constants are defined in Table 2.

Table 2. Constants used in the second-order model equations

$C_{\varepsilon 1}$	$C_{\varepsilon 2}$	σ_k	σ_ε
1.44	1.92	0.82	1.0

The boundary conditions related to this physical problem were described in Table 3.

Table 3. Boundary conditions.

Boundaries	Velocity	Temperature	Mass Fraction	Kinetic energy	Rate of dissipation
chimney	$\tilde{u}=0$, $\tilde{v}=v_0$, $\tilde{w}=0$	$\tilde{T}=T_0$	$\tilde{F}=F_0$	$k_0=10^{-3}u_0^2$	$\varepsilon=k_0^{3/2}/0.5d$ [36]
Wind flow	$\tilde{u}=u_\infty$, $\tilde{v}=0$, $\tilde{w}=0$	$\tilde{T}=T_\infty$	$\tilde{F}=0$	$k_\infty=5.10^{-3}u_\infty^2$	$\varepsilon=k_\infty^{3/2}/0.2$ [36]
Obstacles and ground floor	$\tilde{u}=0$, $\tilde{v}=0$, $\tilde{w}=0$	$\frac{\partial \tilde{T}}{\partial n}=0$	$\frac{\partial \tilde{F}}{\partial n}=0$	$k=0$	$\partial\varepsilon/\partial y=0$
Other faces of the field	$\partial\tilde{u}/\partial n=0$, $\partial\tilde{v}/\partial n=0$, $\partial\tilde{w}/\partial n=0$	$\frac{\partial \tilde{T}}{\partial n}=0$	$\frac{\partial \tilde{F}}{\partial n}=0$	$\partial k/\partial n=0$	$\partial\varepsilon/\partial n=0$

The elevated circular jet with diameter d emits a fume with an ejection velocity v_0 equal to = 8 m s^{-1}. This flow is subjected to a various crossflow velocity u_∞. The Reynolds number based on the diameter of the jet is Re=5000. The temperature of air ambient T_∞ is 293.15 K and the fume temperature T_0 is 343.15K. The Grashof number is given by $Gr_d=\frac{g\beta(T_0-T_\infty)d^3}{\upsilon^2}$ and equal to 7 10^3. The ratio Gr_d/Re^2 is extremely small (= $2.8.10^{-4}$) [37]. This small ratio implies that the effect of buoyancy is negligible and thus that temperature acts only as a passive contaminant. The temperature and concentration are considered as passive scalars.

The flow topology necessitated very fine meshing in a large part of the configuration domain. A non-uniform mesh, extremely tight in the proximity of the chimney, the obstacle and the ground was chosen in order to accurately describe all parameter variations. Table 4 summarized the different values adopted of the mesh in the different parts of the domain.

Table 4. Grid steps in different locations of the domain.

Direction		Δ	α_x	Δy	Δz
Longitudinal	Upstream of the chimney	0.008	0.98		
$x_{i+1}= x_i+\alpha_x\Delta$	Near the chimney and the obstacle	0.001	1		
	Downstream of the obstacle	0.006	0.98		
	Near the ground			0.001	
	Around the chimney and the obstacle			0.003	
Transverse	Far from the upper obstacle face			0.007	
Lateral					0.004

The grid layout in the region between the elevated jet and the obstacle was specified to be finer than that in the downstream region. A grid independence assessment was conducted through three different meshes. A coarser grid of 216 ×130 ×35 in the x, y and z directions respectively, a second finer grid of 250×145×40 which was refined in the vicinity of the jet exit and around the obstacle and a third grid with a large number of cells added in the vertical and lateral directions, yielding 250×155×50 cells were tested. Figure 6 represented longitudinal and vertical velocity profiles for the three picked meshes at x /d= 5 and for v_0 = 8m/s (the Reynolds number based on the chimney diameter d and ejection velocity v_0, $\mathrm{Re} = \frac{v_0 d}{\upsilon}$ =5000) and u_∞=5m/s (The Reynolds number based on the height of the blowing section and crossflow velocity u_∞, $\mathrm{Re}_{\square} = \frac{u_\infty \square}{\upsilon} = 9.4\ 10^4$). The grid independence assessment showed that experimental data is quite predicted by Mesh 3. Therefore, the calculations were carried out with 250×155×50 grid for all the cases.

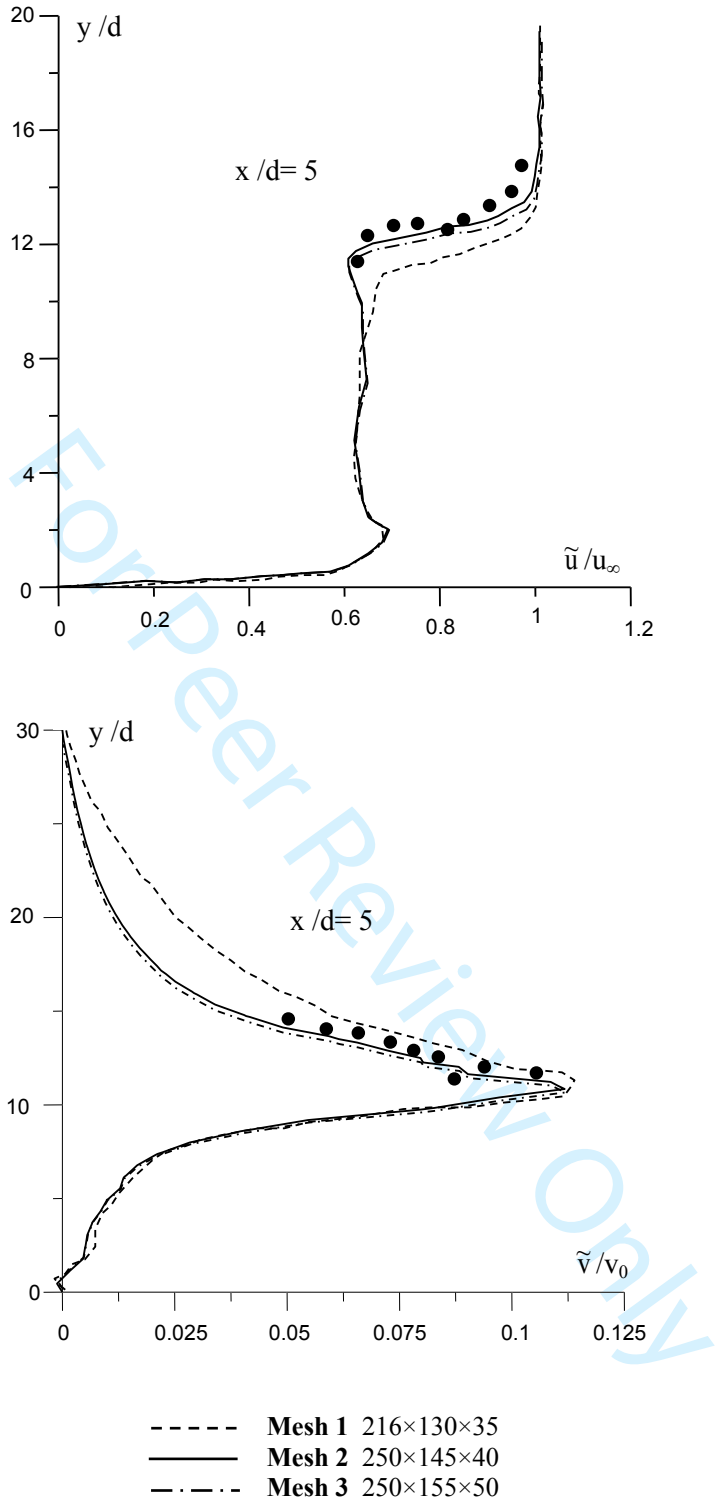

Figure 6. Mesh sensitivity analysis

The numerical code employed the finite volume method based on the SIMPLER algorithm [38]. The implicit scheme was implied for the resulting algebraic equations. The Gaussian elimination method linked to an under-relaxation technique was utilized to compute the obtained tri-diagonal matrix (Table 5).

Table 5. Settings of model

Items	Settings
Turbulence model	Reynolds Stress Model (RSM) with constants given in Table 2
Discretized method	Finite volume Method
Numerical method	The implicit scheme was implied for the resulting algebraic equations
Convergent criteria	The iterative cycle was terminated when the following convergence criterion is established. $\left\|\frac{f^{n+1}-f^{n}}{f^{n+1}}\right\| \leq 10^{-5}$ In the previous equation, f represented the velocity components, turbulent kinetic energy and dissipation rate, while n is the iterative number.

RESULTS AND DISCUSSION

First of all, the experimental results were presented and then the validation of the numerical approach was performed by comparing predicted results to experimental data in several positions and for different parameters. After the choice of the turbulence model, heat and mass transfer analysis of pollutants ejected from a punctual source was carried out.

The effect of the wind velocity on turbulent structures was illustrated in Figure 7 for three velocity ratios between the chimney ejection and the wind source ($R = v_0/u_\infty$). The tested values of the velocity ratio were R = 1.6, R = 1 and R = 0.67 for $Re_\ell = 9.4\ 10^4$ (u_∞ = 5 m/s), $Re_\ell = 1.5\ 10^5$ (8 m/s) and $Re_\ell = 2.25\ 10^5$ (12m/s), respectively. To show the global evolution, we present three images correspond to different times in each velocity ratio (R). Turbulent structures are clearly observed at the exit of the chimney for the different velocity ratios which are called Kelvin-Helmholtz instability. This phenomenon consists of shear layer instabilities of surfaces separating the two fluids moving with different velocities leading to a "vortex sheet" formation on the border between the two fluid flows. From Figure 7, these turbulent structures are found to rotate in one direction or in the other. In fact, the direction of rotation depends on the ratio R between the ejection velocity and the wind velocity. For R = 0.67, it is shown the existence of clockwise rotating vortices imposed by the transverse flow whose velocity is higher than that of the injection. For R = 1 when the velocities of the two flows are equal, bi-

directional vortices are observed giving rise to instabilities formation which in turn lead to other vortices having also two directions of rotation. This results in regular "mushroom" shaped vortices. For the case of R=1.6, the interface instability generates vortices with a counterclockwise rotational direction, as shown in Figure 7.

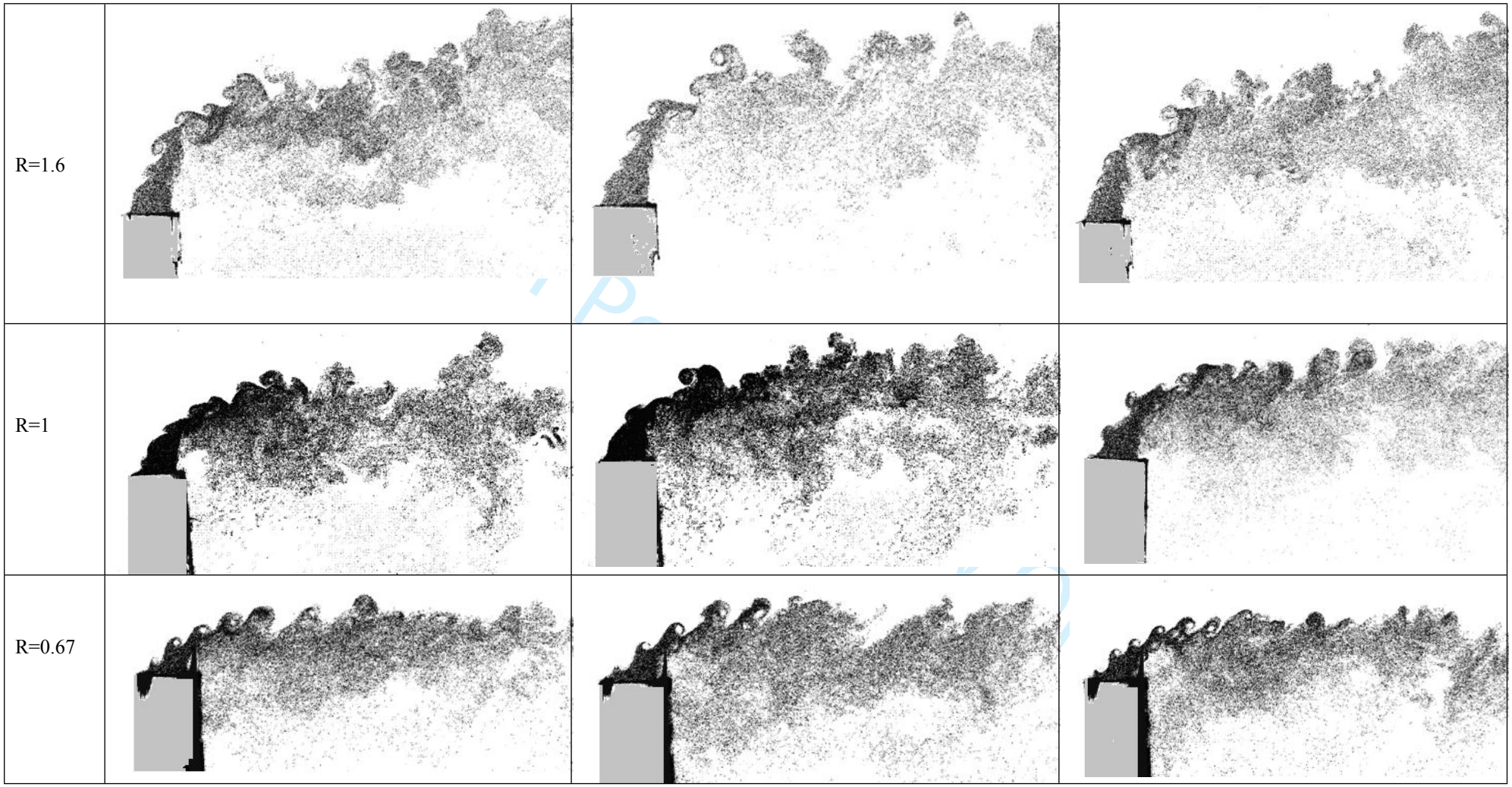

Figure 7. Effect of the wind velocity on turbulent structures

The behavior of a plume discharged from a stack with a velocity of v_0 = 8m/s (Re=5000) and exposed to various free stream ($Re_\ell = 9.4\ 10^4$ (u_∞ = 5 m/s), $Re_\ell = 1.5\ 10^5$ (8 m/s) and $Re_\ell = 2.25\ 10^5$ (12m/s)) was depicted in Figure 8 in cases of absence and existence of a cylindrical obstacle. The complex flow behavior was a consequence of the interaction between the downflow effect, which is initiated by the crossflow induced by the stack outlet, the upward shear impact generated by the outflowing plume, and the wakes behind the plume, the stack and the obstacle.

This visualization allowed us to see that the surrounding flow strongly influences the plume flow. The major determinant of the plume form is the exit velocity over the wind velocity (velocity ratio). When this ratio is greater than 1, it is possible to differentiate three phases of plume evolution in the ambient surroundings. In the first region: the plume prevails over the flow. In the second region: the exhaust velocity is equal to the crosswind. In this phase, the ejection velocity is equal to the crosswind and the plume starts to curve. In the third and final region, the crosswind is overpowered and the flows are transported towards the wake of the chimney. In summarizing, the image analysis showed the behavior of the plume with and without obstacles.

It is worth noting that the released plumes curved in the direction of the crossflow stream; more the wind velocity was stronger, more the plume was straight (from R = 1.6 to R = 0.67). Downstream of the plume, a wake zone forms in both cases, with or without an obstacle. In the case of a ground source without the presence of an obstacle, this wake region (the plume wake) reacts with the boundary layer at the ground surface. For an elevated source with a flat unobstructed environment, the plume wake reacts with the wake downstream of the stack (stack wake). In the presence of an obstacle, representing a building, the whole flow structure changes. There are two regions of wake behind the chimney and behind the building. In both cases, typical flow patterns are shown in the first plume region coming from the chimney. This analysis also revealed how the obstacle-free plume reaches higher peaks. These image analyses were used to better determine the shape of the plume and especially to specify the inversion layers and their relationship with the obstacle.

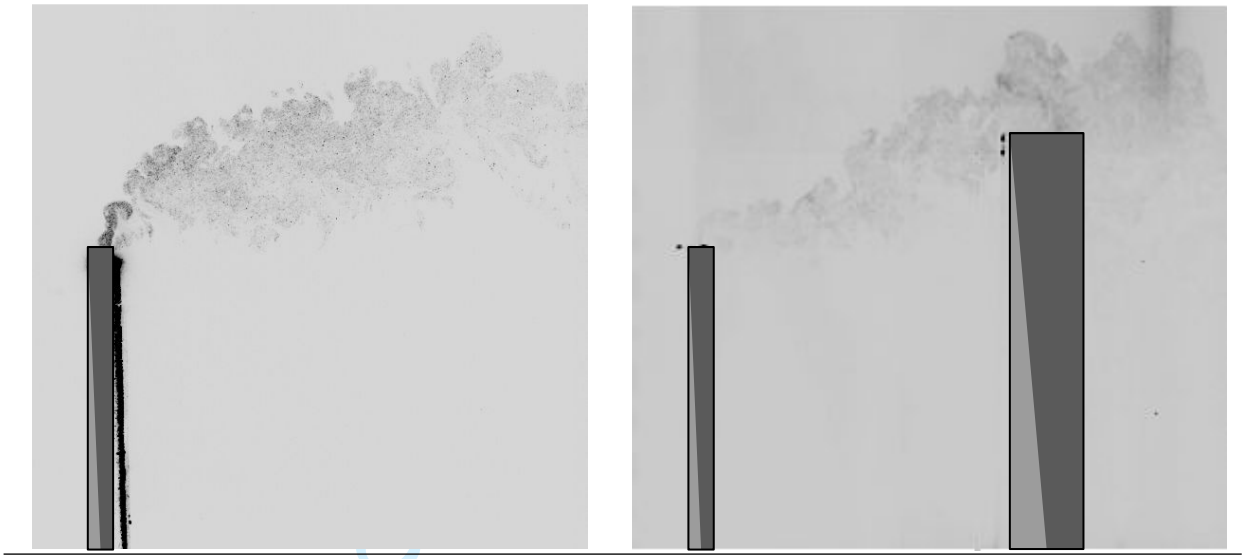

R=1.6 ($Re_\ell = 9.4\ 10^4$)

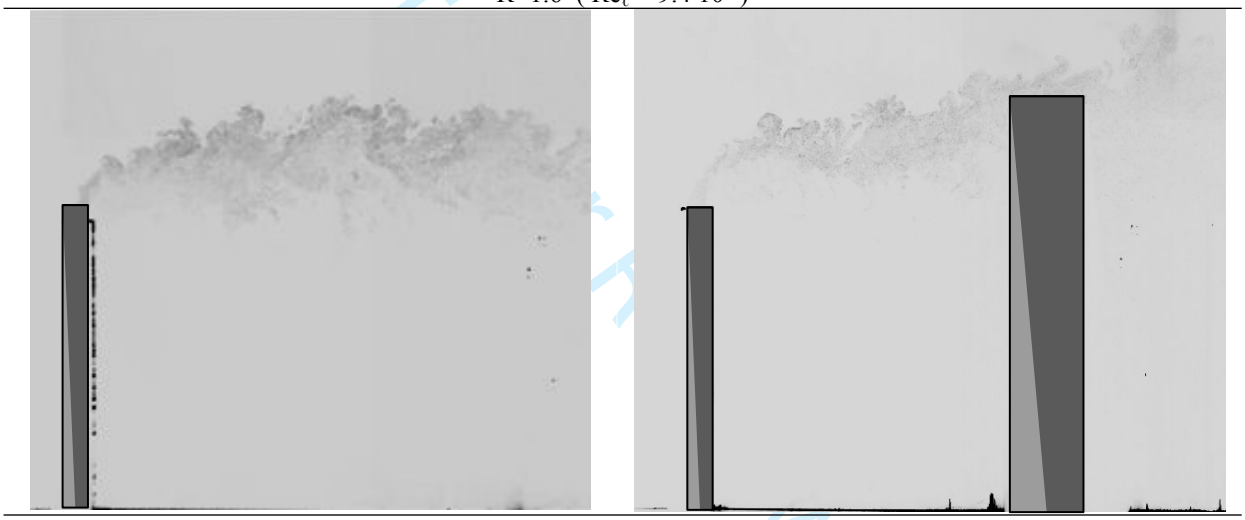

R=1 ($Re_\ell = 1.5\ 10^5$)

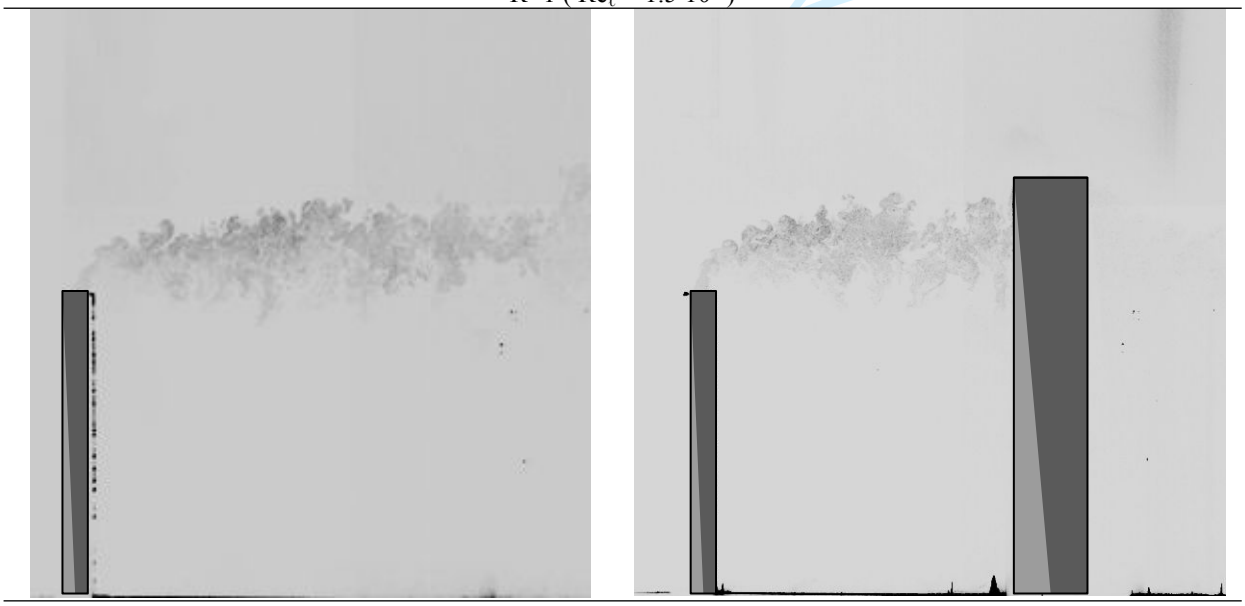

R=0.67 ($Re_\ell = 2.25\ 10^5$)

Figure 8. Effect of the obstacle presence on the plume evolution, Re=5000

Figure 9a depicted the mean velocity vectors in the wake near the building (cylindrical obstacle) in the median plane section. A strong deflection of the fluid behind the building and a saddle point which limits its penetration in the wake were observed. The position of this saddle point varies according to the value of the velocity ratio, but it allows dividing the wake into four regions. Indeed, the upper left region which is the part of the recirculation zone subject to the downflow created by the free end of the building has an unstable focus. The upper right region is the part of the flow outside the recirculation zone and, despite the obvious influence of the recirculation zone, it exhibits upward motion further into the wake due to the contribution of the lateral flow. The third region, located lower left, is the part of the recirculation zone dominated by the influence of the bottom wall. Finally, the fourth region is the zone of the interaction between the bottom wall and the wake.

Figures 9b and 9c showed the vertical and longitudinal components of the velocity (and respectively) for Re=5000 and $Re_\ell = 3\ 10^5$ leading to a velocity ratio less than 1 (R = 0.5). It is clear that the jet emitted by the chimney and seeded by glycerin particles is immediately deflected by the transverse flow (the wind velocity). The transverse flow was not seeded that is why it could not be seen in these figures. An aspiration of the flow is noted behind the chimney. The ejected jet elevation is not very high and the flow distribution is influenced by the presence of the cylindrical obstacle. The stagnant point is located at a height equals to 110mm. A part of the jet flow is trapped between the chimney and the building obstacle and the other part passes over the obstacle. It is worth mentioning that vortices of small dimensions rotating in the opposite direction of the clockwise are developed downstream of the cylindrical obstacle, on its top and on its lateral side, confining the recirculating zone behind the obstacle.

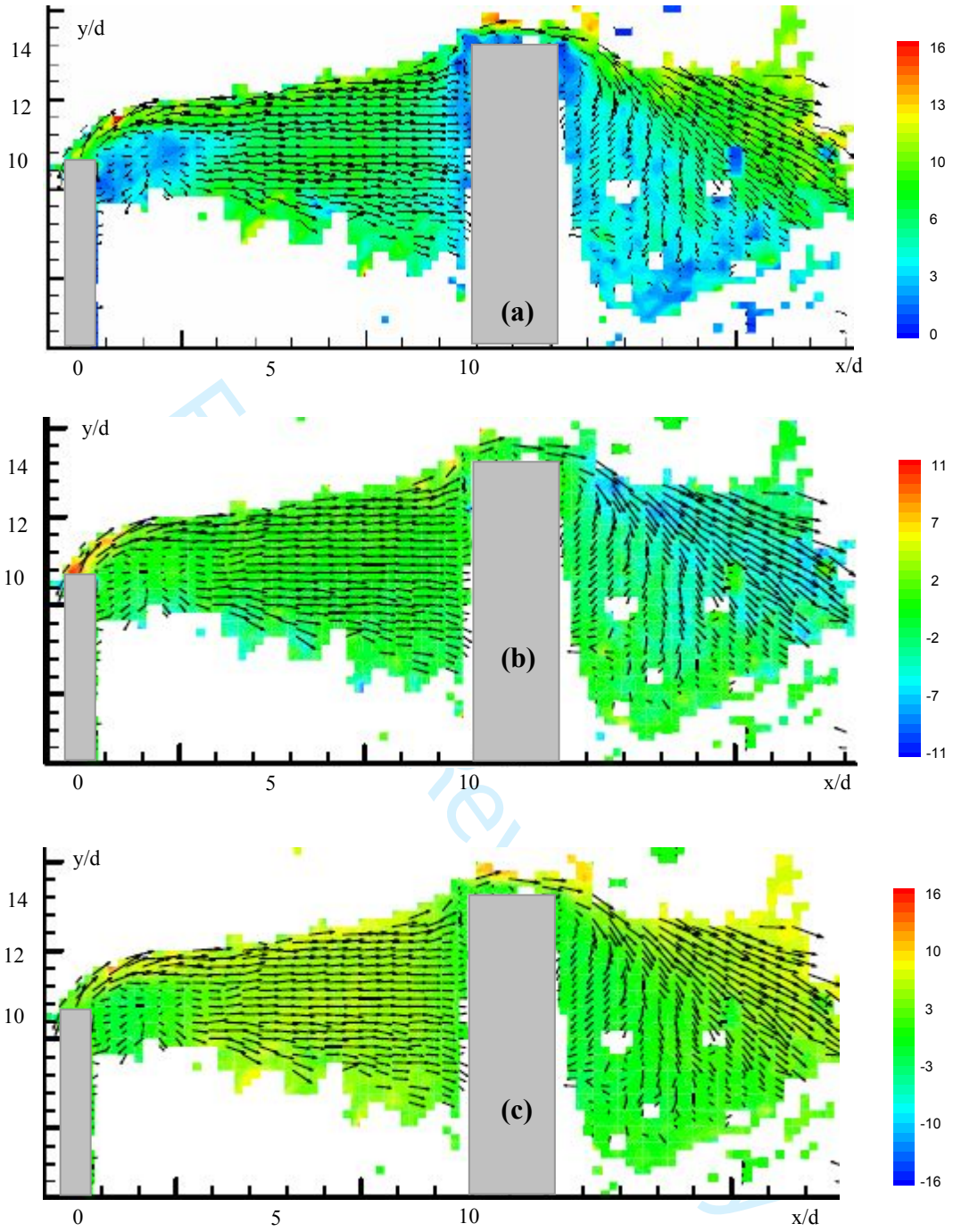

Figure 9. Contours of a) mean velocity, b) vertical velocity component $\overline{v}$ and c) longitudinal velocity component $\overline{u}$ vectors (Re=5000 and $Re_\ell = 3\ 10^5$)

Figure 10 showed the visualization of the plume evolution emitted from the chimney at v_0=8m/s (Re=5000) and exposed to various wind speeds: u_∞=5m/s ($Re_\ell = 9.4\ 10^4$), u_∞=8m/s ($Re_\ell = 1.5\ 10^5$), u_∞=12m/s ($Re_\ell = 2.25\ 10^5$) and u_∞=16m/s ($Re_\ell = 3\ 10^5$). It is noticed that the form of the plume is distinctly influenced by the velocity ratio. When the velocity ratio v_0/u_∞ is higher than 1 (fourth image), it is possible to identify three phases in the evolution of the plume. The first phase corresponds to the jet exit which is practically vertical. The second phase is identified by the weakening of the jet velocity to become equal to that of the upstream flow and by the curving of the jet. Finally, the third stage occurred when the main flow predominates and the plume becomes horizontal. In this case, the free end of the cylindrical obstacle is flushed with the plume and it is noted that the recirculation area behind the obstacle is significant compared to the three others velocity ratios. Also, given the high jet elevation, it is observed that the jet evolution is important above the cylindrical obstacle. For the velocity ratio $v_0/u_\infty = 1$ (third image), the first phase is not apparent. As the vertical velocity of the plume is equivalent to the horizontal velocity of the ambient flow (characteristic of the transition between the 1st and 3rd phase), the plume can be considered to leave the chimney and directly start its second phase. It encounters the obstacle at a height lower than that obtained for a velocity ratio R> 1. In the case of velocity ratio v_0/u_∞ is lower than 1, the first two phases are not seen. The plume only drips in the wake formed by the ambient flow above the chimney. It evolves in line with the ground and around the obstacle at a much lower height compared to the other cases. The higher is the wind velocity, the larger is the recirculation zone downstream of the obstacle.

A recirculation zone is observed on the top of the cylindrical obstacle. It seems to be due to the separation of the fluid arriving on the upstream edge of the cylinder from the chimney. But at high ejection velocity, the separation does not occur directly on the edge but further on the top of the obstacle. The fluid reaching the side surfaces of the building accelerates as it approaches the free edge. Due to the pressure variation between the side surfaces and the top, the fluid has an upward velocity component. Thus, on each side surface, the shear layer rolls up on each side to fold back onto the top and gives rise to the marginal vortices. These vortices, symmetrical on average, contribute to the deflection of the fluid in the wake of the cylindrical building and can alter or even destroy the von Karman vortices.

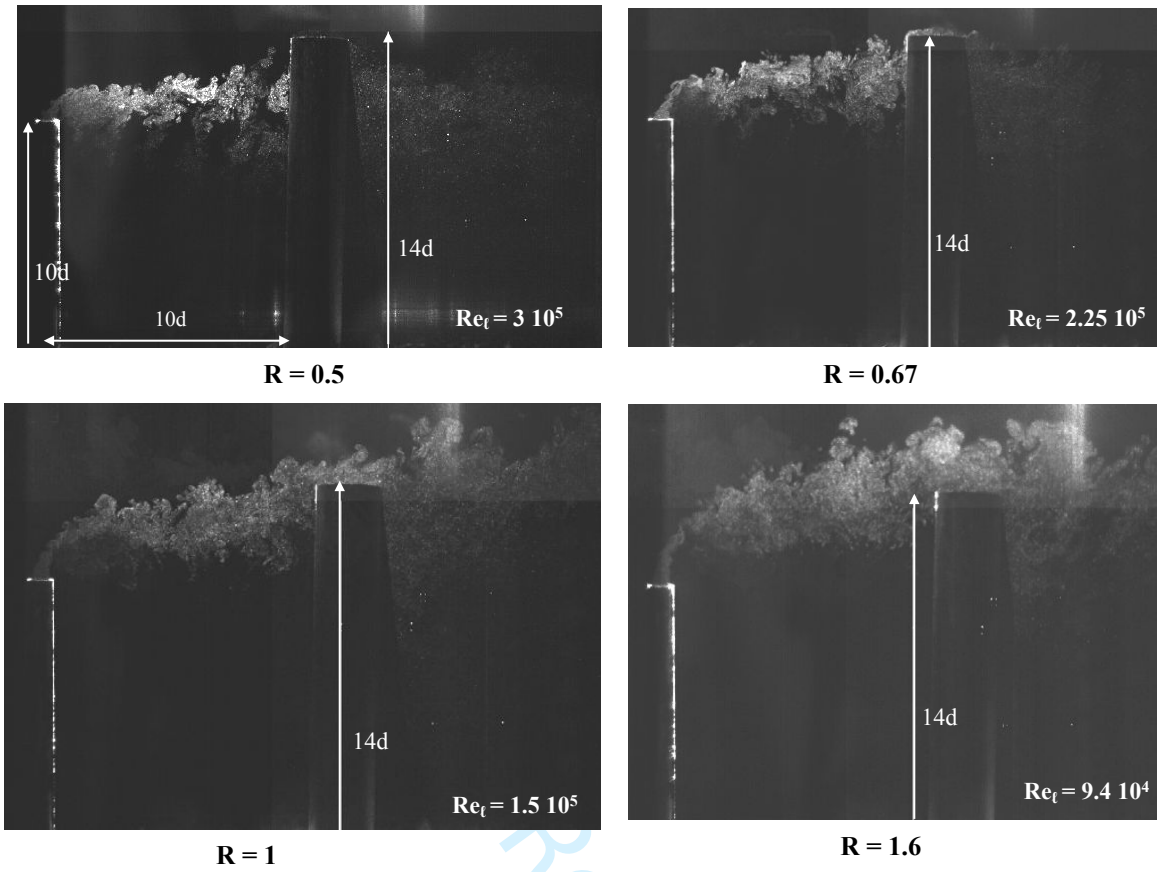

Figure 10. Influence of wind 8velocity on the evolution of the plume emerging from the chimney around a cylindrical obstacle, Re=5000

Velocity vectors of the four velocity ratios cases presented in Figure 11 show that the wind velocity has a pronounced impact on the flow structure. In fact, the flow emerging from the stack tracks the direction of the momentum plume exhausted. Then, it is redirected by the wind velocity and hits the front face of the building, forming a stagnation zone. The height of this latter varies with the value of the wind velocity. The velocity in the stagnant region is quite low, which justifies the low intensity of the vortices developed. At the top of the cylindrical obstacle, it is revealed the existence of a separation zone dominated by a strong swirl for the velocity ratio R=1.6. For the cases of velocity ratios R=1 (v_0=8 m/s and u_∞=8m/s) and R=1.6 (v_0=8m/s and u_∞=5m/s), it is remarked that a small recirculation region is formed in the building upper face. In this region, the flow separated from the upstream edge of the cylindrical construction connects to the roof at a distance downstream from this boundary. The flow returns to the interior of the separation bubble with high degrees of turbulence. The wake of the upper surface of the building includes both recirculation and high turbulence regions. In the downstream region, behind the rear face of the obstacle, there are recirculation zones with different sizes depending on the velocity ratios. The flow is entrained into a big recirculation region in the case of R = 0.5.

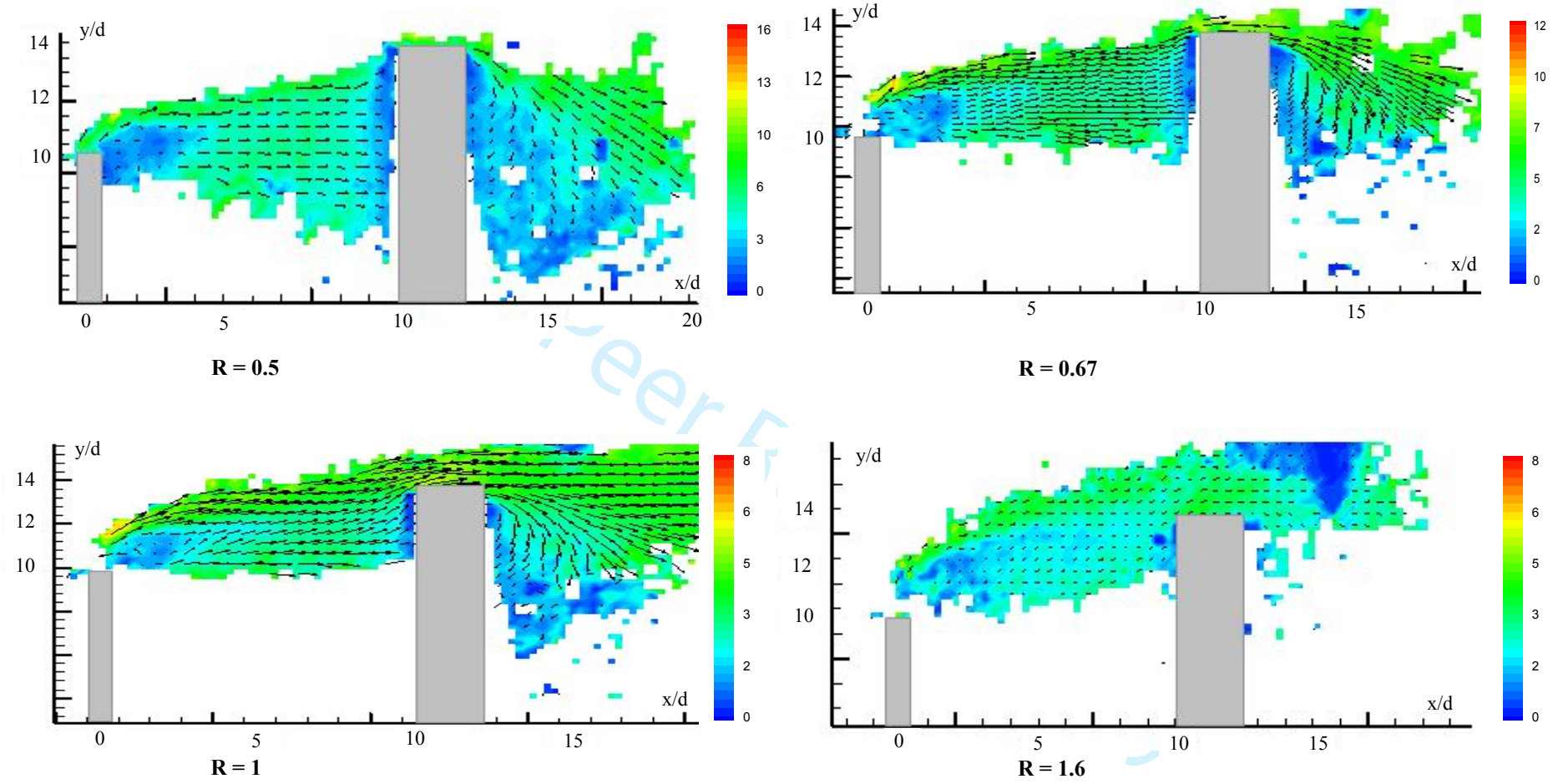

Figure 11. Velocity vectors for various velocity ratios in the presence of a cylindrical obstacle

In order to extent the investigation of the chimney flow behavior behind a cylindrical building numerically, it was mandatory to validate the turbulence closure model by confronting predicted results with experimentally collected data. Simulations were performed using the RSM model and covered both mean and turbulent features. Longitudinal and vertical distributions of the dynamic field in various streamwise emplacements of the flow field were considered. The first position was x/d = 5 which represents the halfway between the stack and the cylindrical obstacle. The second position was x/d = 11 situated in the middle of the building. The third position was x/d = 16 located in the recirculation region downstream of the cylindrical obstacle. The plume was ejected at a fixed velocity value u_0=8m/s (Re = 5000) and under a wind velocity u_∞=8m/s ($Re_\ell = 1.5\ 10^5$).

Figures 12 and 13 illustrated predicted and measured results of the longitudinal $\tilde{u}$ and vertical $\tilde{v}$ velocities at the three selected locations of the domain as a function of the vertical coordinate (y) for R=1. The experimental data was compared to the numerical simulation results achieved by the second-order model (RSM). The accordance between experimental and numerical findings is considered acceptable with an averaged error of 5% for both velocity components. For the mean vertical velocity profiles in the first axial position, the influence of the obstacle's presence is not important in this position. The shape of the evolution has a Gaussian profile. The results at the second position and in the downstream region show the presence of two peaks (one positive and one negative) which is the result of recirculation zones. The important negative peak is located at the end of the obstacle for these both latter locations.

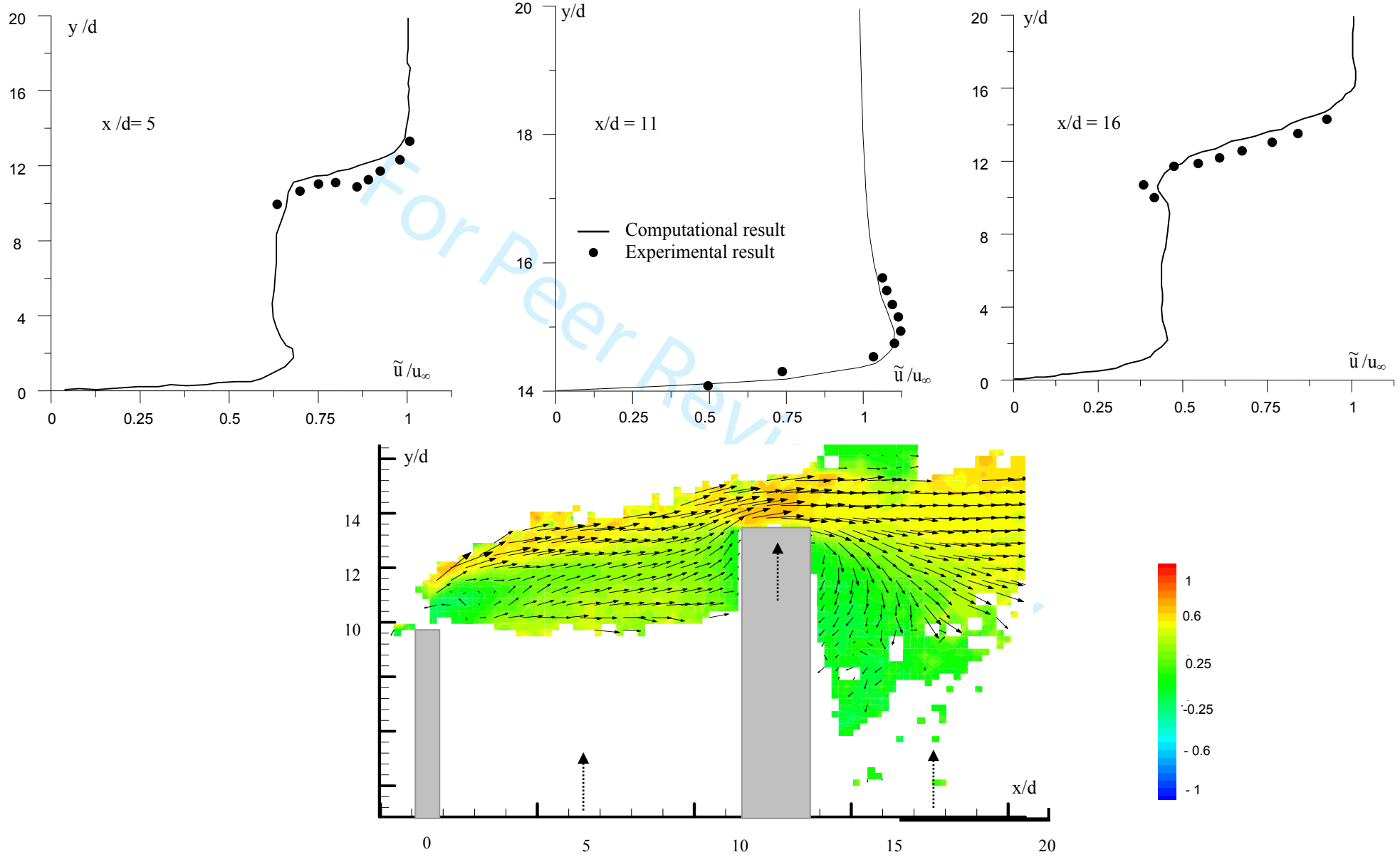

Figure 12. Mean longitudinal $\tilde{u}$ velocity profiles at R=1

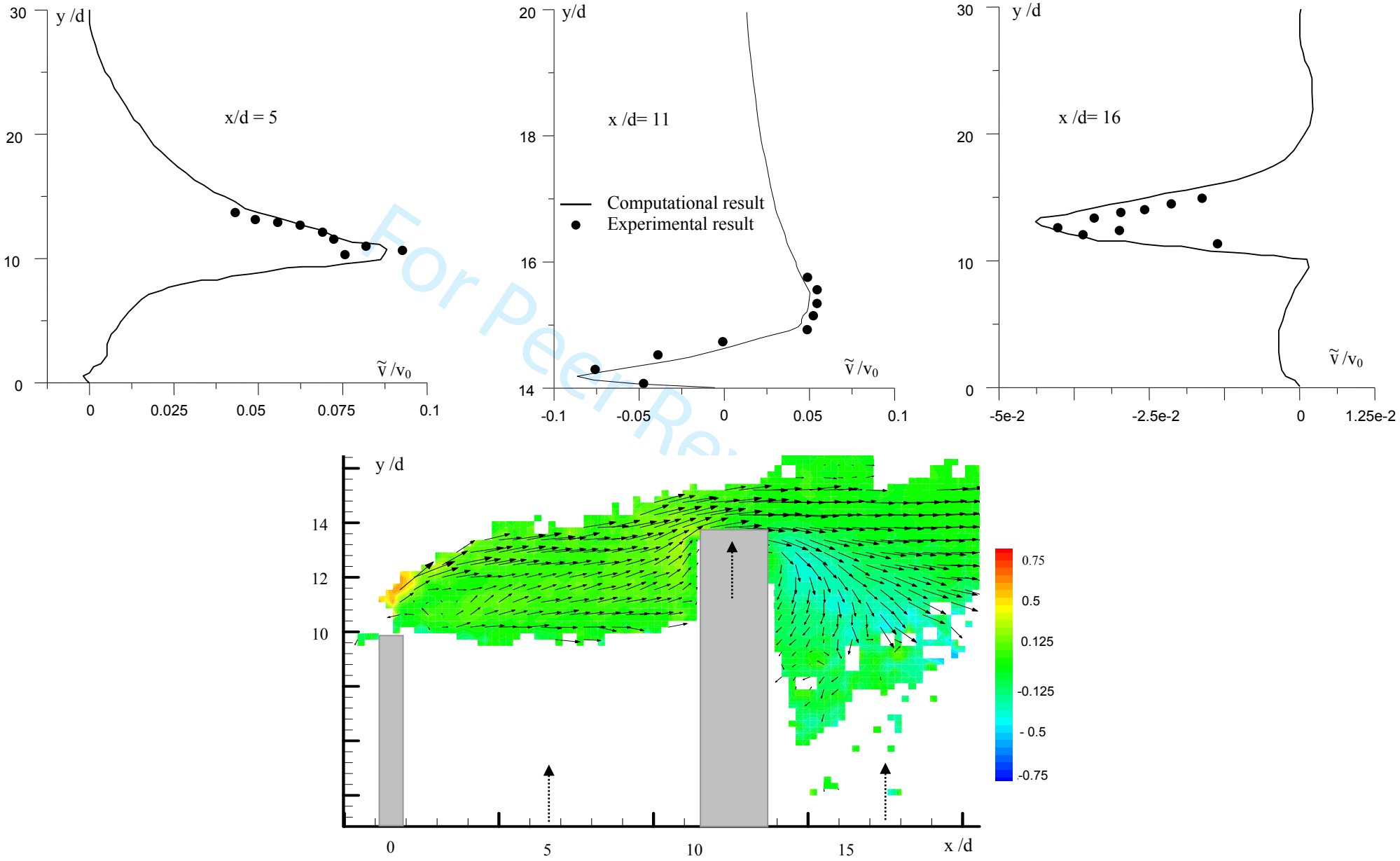

Figure 13. Mean normal $\tilde{v}$ velocity profiles at R=1

The computed Reynolds stress $\frac{\overline{u''u''}}{u_\infty^2}$ and $\frac{\overline{v''v''}}{v_0^2}$ and the experimental data were compared in Figure 14 at different locations (x/d=5, x/d=11and x/d=16) and at Re=5000 and Re_ℓ=1.5 10^5 (R = 1). It is obvious that there is a qualitative match between horizontal and vertical stresses and a satisfactory agreement between experimental and computational results. However, the averaged error between measured and simulated data is about 17% which is higher than that for mean velocities.

Upstream of the cylindrical obstacle (x/d=5), the fluctuating turbulent velocities are very high with reference to those calculated above (x/d=16) and downstream of the building (x/d=16). In fact, the horizontal and the vertical fluctuation components, $\frac{\overline{u''u''}}{u_\infty^2}$ and $\frac{\overline{v''v''}}{v_0^2}$, attain maximal values of approximately (2.8 10^{-2}) and (1.06 10^{-2}), respectively upstream of the building. Whereas in the top of the building, the peak values of the horizontal and vertical Reynolds stresses are about (6.87 10^{-3}) and (2.03 10^{-3}), respectively. In downstream of the building, the peak value of the horizontal Reynolds stresses is about (8.91 10^{-3}) and those of vertical Reynolds stresses is (7.34 10^{-3}). Far downstream, the horizontal and vertical stress ends seem to disappear when leaving the interaction area.

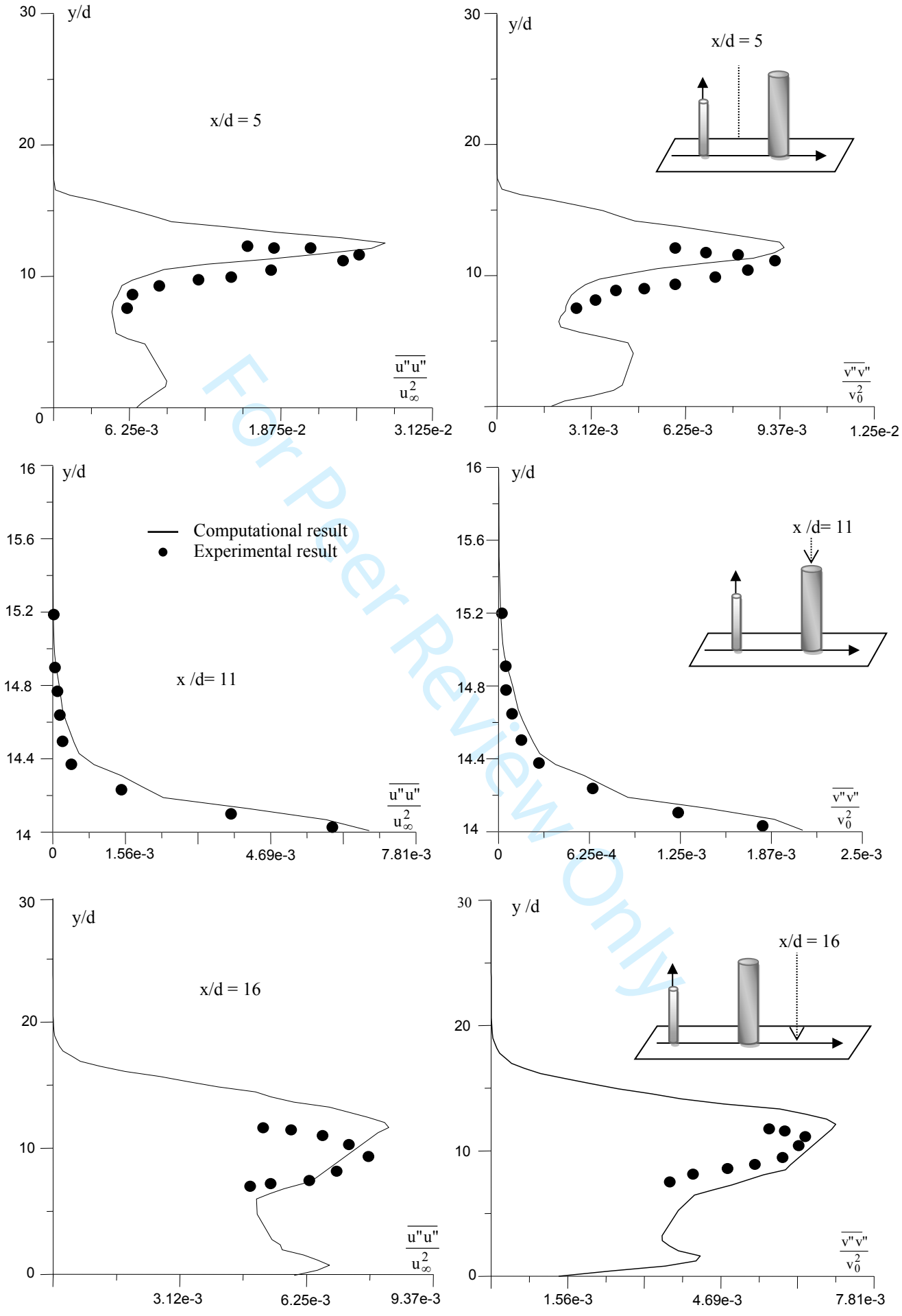

Figure 14. Horizontal and vertical Reynolds stress at different streamwise locations

Figure 15 displayed velocity contours of the pollutant ejected from an elevated jet (mock-up model of an industrial chimney) at Reynolds number Re=5000 and under various Reynolds numbers Re_ℓ (Re_ℓ =3 10^5, Re_ℓ=1.5 10^5, Re_ℓ =9.4 10^4) in different cross-sectional planes. The first cross-sectional plane was the horizontal XZ plane located at the mid chimney height (y/d=5), the second plane was fixed at the level of the chimney exit (y/d=10) and the last one was set over the whole mock-up at y/d=16. A narrow band of descending movement along the centerline of the wake downstream region of the obstacle is noticed. This disappears at the last cross-sectional plane (y/d=16). Interspersed filaments of rising and falling pollutants spread externally from the wake centerline in a V-shaped pattern. These filaments are footprints of vortex structures that move with the mean flow. The dimension of this vortex increases with the wind velocity (u_∞= 16 m s^{-1}, Re_ℓ =3 10^5) as it is clearly shown in the lateral plane y/d = 10. This latter depicts the impact of the wind velocity. As can be seen, the different turbulent structures were successfully presented, indicating the existence of organized stationary movements, such as the horseshoe vortex around both the base of the elevated jet (chimney model) and the cylindrical building model and the recirculation vortex at the lee side of the obstacle. It is obviously illustrated by these figures the presence of the horseshoe vortex and the marginal vortices which originate at the top of the cylinder but which, further in the wake, amalgamate with the lateral flow to form the trailing vortices. The fluid below the stagnation height (depending of the velocity ejection) goes almost horizontally through the cylindrical obstacle and splits off from the limit in an essentially two-dimensional way (distinctly shown in y/d= 5 and y/d = 10 planes, for all velocity ratios). This separation of the boundary layer in almost lateral planes has often been invoked to describe the heeded eddies circulating around vertical axes in wakes. The recirculation zone over the upper face of the building is clear in the lateral plane y/d= 16 and its size is important for the ambient velocity u_∞= 5ms^{-1} correspondent to Reynolds number Re_ℓ =9.4 10^4.

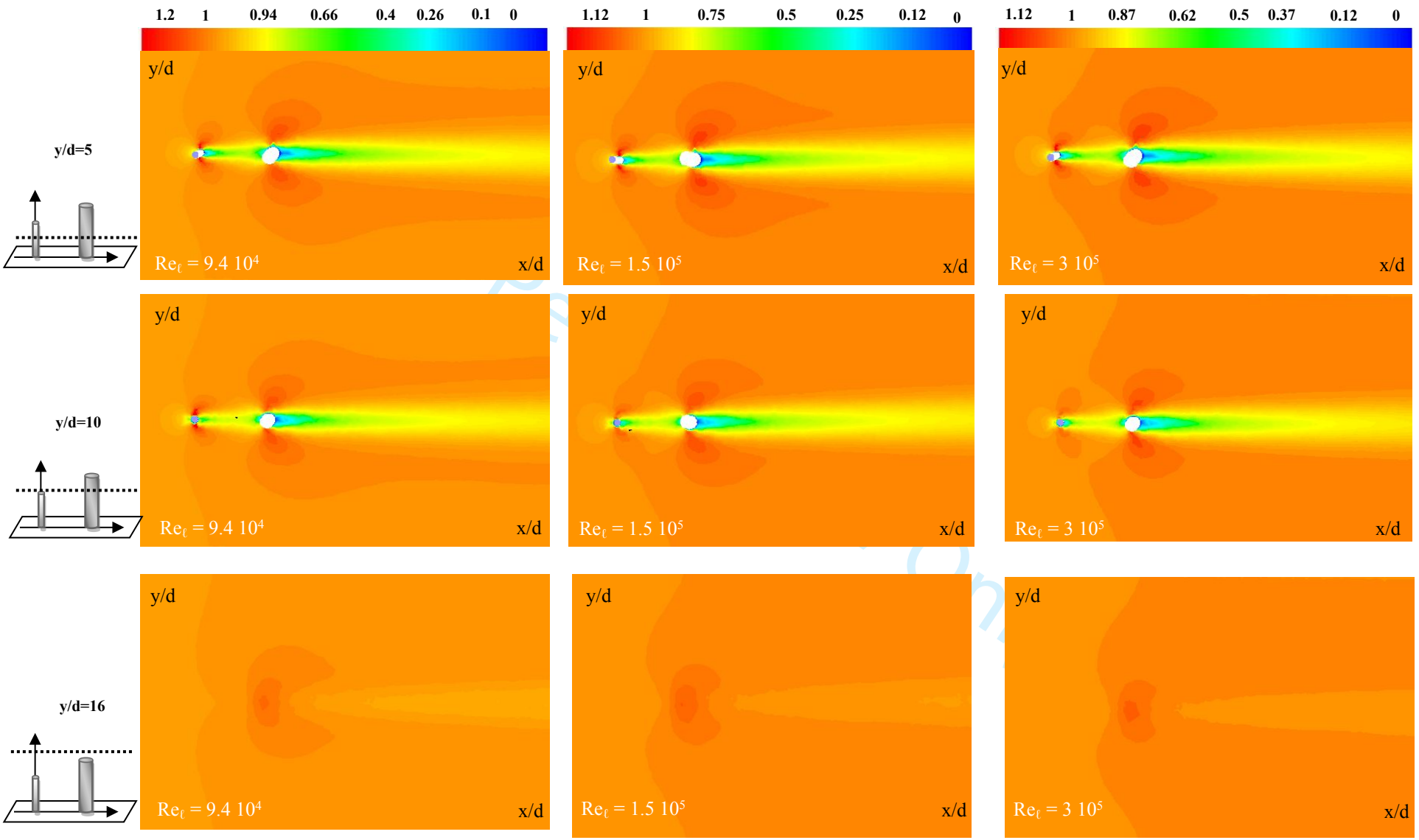

Figure 15. Mean velocity contours of the global chimney jet' progression around the cylindrical obstacle at different lateral planes and under different wind velocities and Re = 5 10^3

The variation of the Strouhal number with Reynolds numbers ($Re_d = \frac{u_\infty d}{\upsilon}$ and $Re_D = \frac{u_\infty D}{\upsilon}$) are presented in Figure 16. The range of Reynolds number applied is within 3125 and 20000. The Strouhal numbers decreased as the Reynolds number increased. The calculated Strouhal numbers agreed to the experimental results found by Roshko [39, 40] at the same Reynolds numbers [41].

The static pressure coefficient (Cp) on the chimney and the obstacle is shown in Figure 17. For both chimney and obstacle, predicted pressure coefficients on the centerline plane (z/d=0) of windward and leeward facades are presented. For the windward facades, the pressure coefficient of the cylindrical obstacle was weaker compared to those of the chimney because at the entrance the air is accelerated. On the other hand, Figure 17 (b) shows that the leeward pressure coefficient of the chimney façade was much smaller than the leeward pressure for the obstacle. In the region between the chimney jet and the cylindrical obstacle, the crossflow is trapped, that's why it is illustrated the leeward coefficient pressure smaller than the upstream Cp. Altogether, this figure imply that the pressure difference between the windward and leeward façades (the driving force for cross ventilation) of short obstacle (we can consider the chimney as an obstacle) was higher than that for long obstacle (cylindrical obstacle). In other words, the ventilation rate of short obstacle will be larger than that of long obstacle.

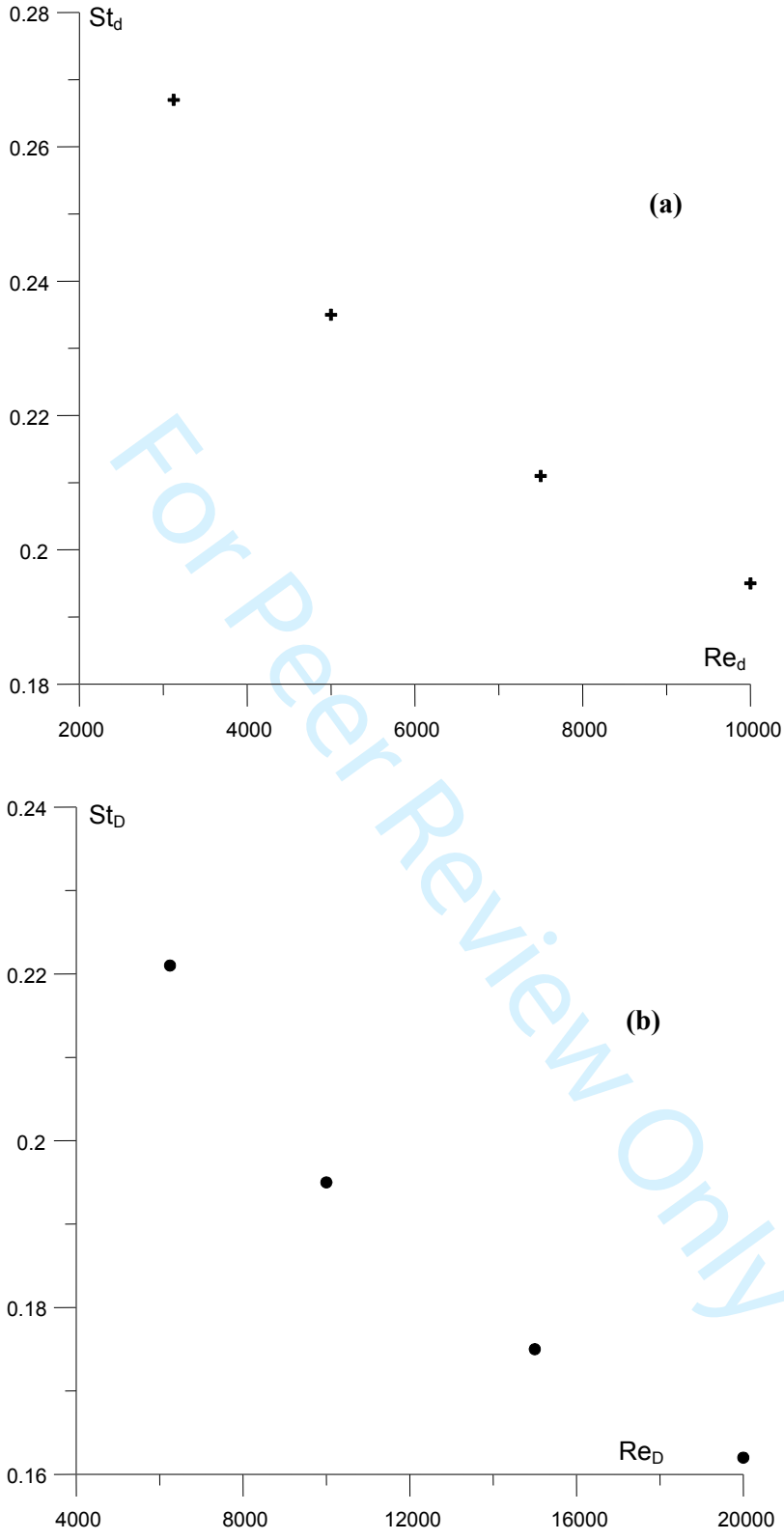

Figure 16. Strouhal vs. Reynolds number for the chimney (a) and the obstacle (b)

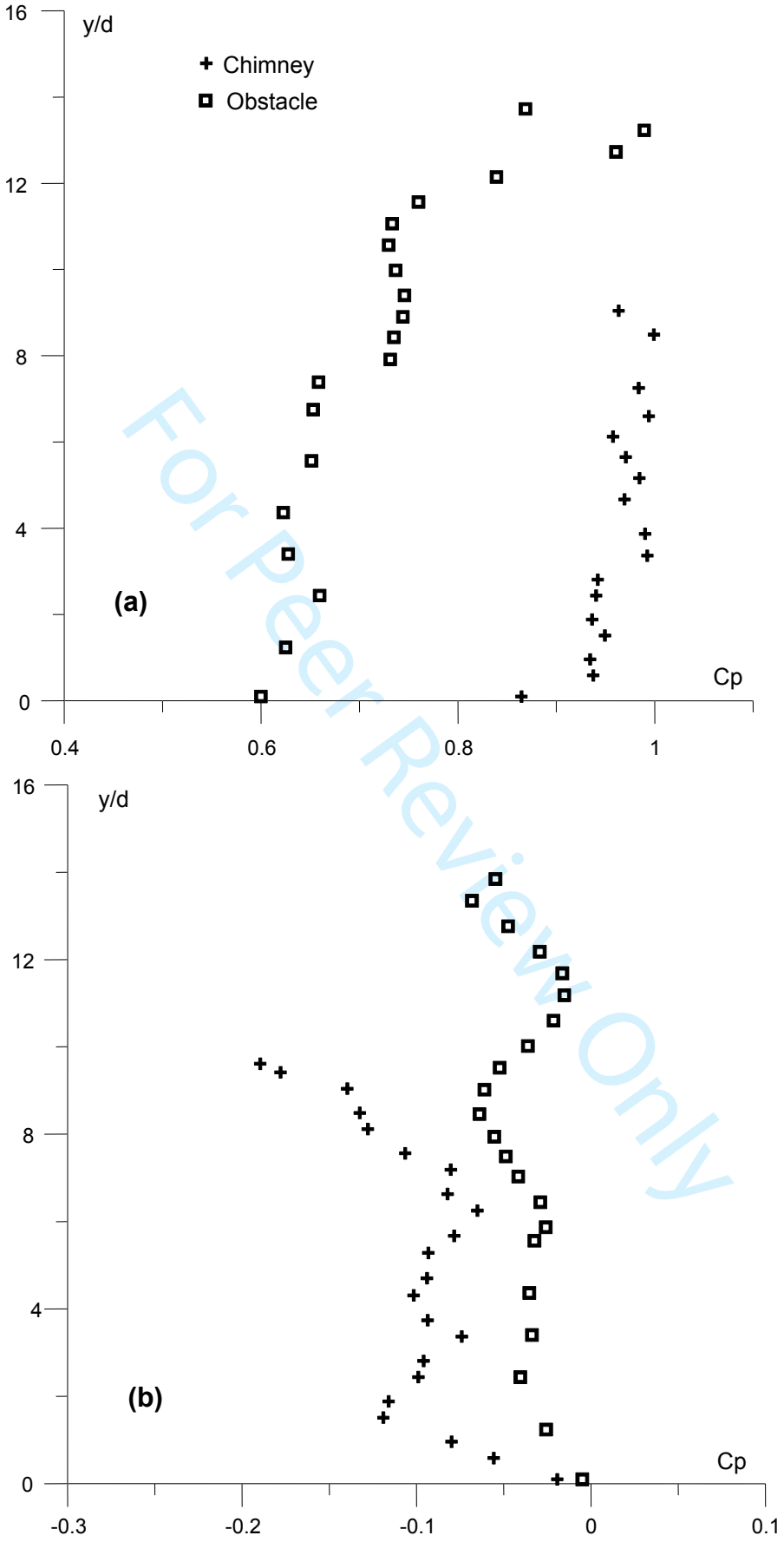

Figure 17. Pressure coefficients on the center plane (z=0): (a) windward facade; (b) leeward facade.

After treating the dynamic behavior of the flow field, the discussion would be devoted to the thermal aspect and the dispersion of the CO_2 pollutant ejected from the chimney at a temperature T_0 =343.15K within the environing air mainstream (T_∞ =293.15K). Figure 18 depicted the lateral distribution of the pollutant temperature at successive y cross sections. The considered planes were situated above the chimney at mid height (from y/d=7 to y/d = 10) which reflected the downwash behavior of the pollutant and over the chimney exit (y/d=10.1 to y/d= 15) due to the interesting phenomena it yields: the extension of the rear plume, the ascension of the plume around the cylindrical obstacle and the creation of a trapped flow behind the obstacle in the downstream region. The results shown in Figure 18 clearly indicated that the flow separates at the front edges of the cylindrical obstacle, resulting in severe separation vortices. The principal characteristic is the two horseshoe structures created in front of the face chimney pipe and in front face of the obstacle as a consequence of the adverse pressure gradient. The vortex is deviated downstream following the lateral faces of the cylindrical obstacle. The horseshoe vortex system upstream of the obstacle and the two enormous vortices separating each side of the obstacle are perceptible at various lateral planes. The vortices separated on the sides approach the back of the obstacle. Within the rear chimney nozzle, there is a decreasing profile starting from an initial pollutant temperature value until reaching the environment temperature. This initial value is reasonably distinct as the temperature of pollutants are cooled by the cross flow.

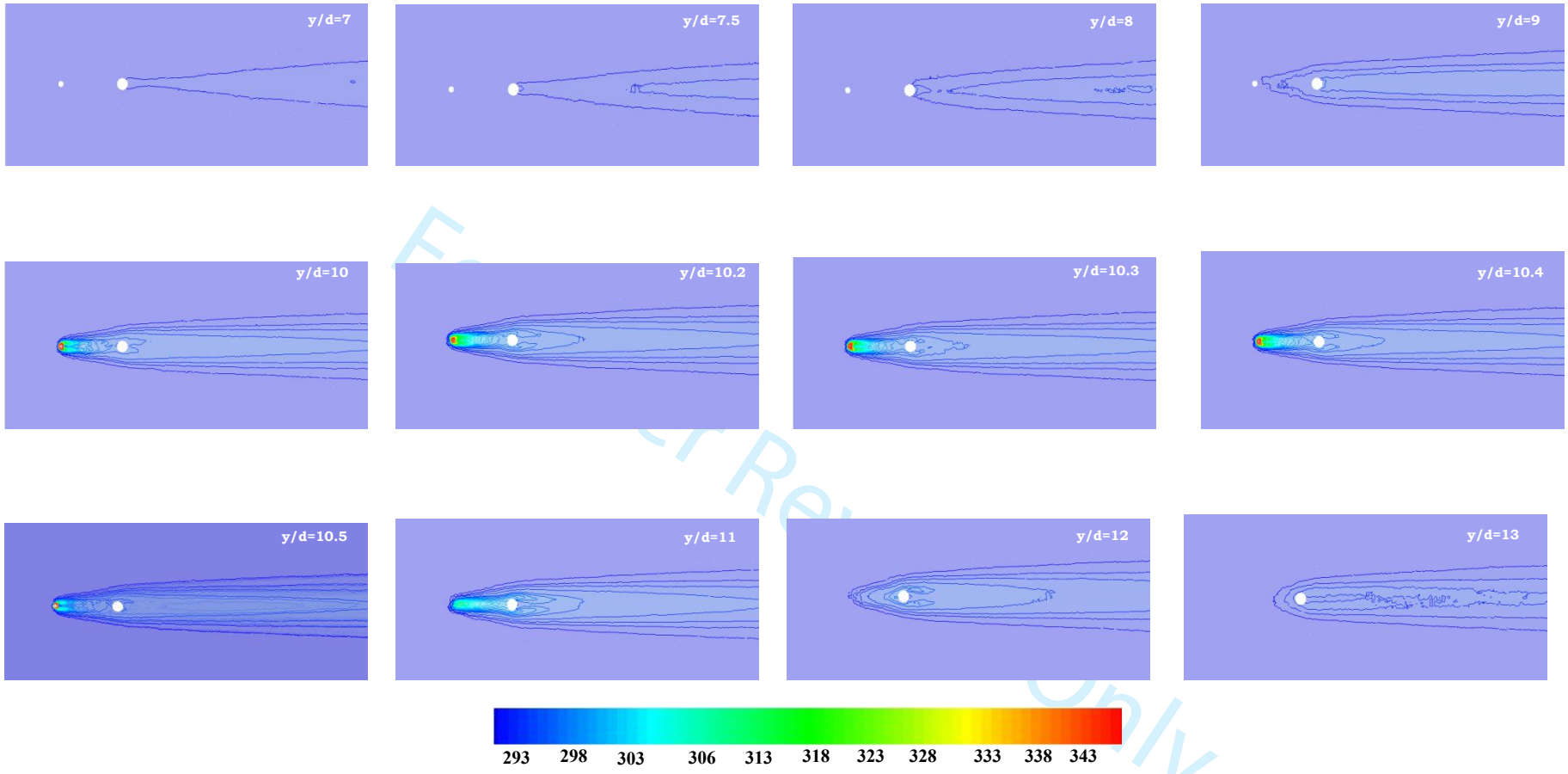

Figure 18. Temperature evolution around the cylindrical obstacle at different lateral planes for Re=5000 and $Re_\ell = 3\ 10^5$

It would be useful to examine how the velocity ratio influences the heat transfer process in the presence of the cylindrical obstacle. Averaged isotherms contours around the cylinder were displayed in Figure 19 for various velocity ratios; R=1.6, R=1 and R=0.5 corresponding to $Re_\ell = 9.4\ 10^4$, $Re_\ell = 1.5\ 10^5$ and $Re_\ell = 3\ 10^5$, respectively and for Re=5000. This figure revealed that the isothermal contours are affected by the wind velocity u_∞. Indeed, the temperature penetration depth in the principal flow decreases over the upper surface of the obstacle as the wind velocity u_∞ grows (Table 6).

Table 6. Maximum values of Temperature on the upper surface of the cylindrical obstacle.

	R=0.5		R=1		R=1.6	
X position	x/d=10	x/d=12	x/d=10	x/d=12	x/d=10	x/d=12
Y position	y/d=14.1	y/d=14.1	y/d=14.1	y/d=14.1	y/d=14.1	y/d=14.1
Temperature	T=293.24K	T=293.22K	T=295.1K	T=294.7K	T=299.7K	T=299.1K

The larger deflection of the lower shear layer, followed by stronger recirculation zone, with increasing the wind velocity u_∞, extends the penetration depth in front of the upstream face of the obstacle. Similarly, the temperature penetration depths over the obstacle front face are influenced by the velocity ratio, as recapitulated in Table 7.

Table 7. Maximum value of Temperature over the front face of the obstacle.

	R=0.5	R=1	R=1.6
X position	x/d=10	x/d=10	x/d=10
Y position	y/d=11	y/d=12	y/d=14
Temperature	T=298K	T=300K	T=301K

The maximum temperatures downstream the rear surfaces of the obstacle were described in Table 8 for different velocity ratios R. It was worth noting that the temperature of the pollutant in the ground is not significantly affected by the velocity ratio R.

Table 8. Maximum value of Temperature in the downstream region of the obstacle.

	R=0.5	R=1	R=1.6
X position	x/d=14.5	x/d=14	x/d=12.5
Y position	y/d=11	y/d=12	y/d=14
Temperature	T=295.5K	T=297.5K	T=301K

The pollutant could be a fume ejected by a mockup of industrial chimney. The non-reactivity of the fume allowed envisaging a single pollutant as for example, CO_2. The observations found based on the CO_2 species behavior will stand valid for other examples of pollutants. Thus, in the following, the Carbone dioxide was considered as a pollutant evolving from a chimney in order to follow its progress throughout the field in the presence of cylindrical building (cylindrical obstacle).

Figure 19 shows the profiles of the mass fraction of carbon dioxide in the central plane for several longitudinal positions x/d (in front of the obstacle, for x /d= 5, on the roof in the middle of the obstacle, for x /d= 11, just downstream of the rear edge, for x/d =20, and, finally, downstream of the obstacle, for x/d=30, x/d=35, and x/d=40) as a function of the normal y/d coordinates for different velocity ratios R=1 (Re=5000 and Re_ℓ=1.5 10^5), R=0.67 (Re=5000 and Re_ℓ=2.25 10^5) and R =0.5 (Re=5000 and Re_ℓ=3 10^5). The evolution of the pollutant before the obstacle and in the vicinity of the obstacle is examined. For the zone located between the chimney and the obstacle x/d =5, the mass fraction of the pollutant is maximum. The profile is Gaussian, the level of the maximum is higher than the height of the chimney and this is due to the preponderance of the ejection velocity in this region. In this region, the plume, still in its first phase of evolution, is guided by its initial inertia. On the roof where x /d= 11, we notice that the maximum concentration is just on the roof and it starts to decrease rapidly (for the three cases) because of the wind velocity which dilutes it rapidly. In the downstream region of the building, the profile of the mass fraction has regained its Gaussian shape. In this area the pollutants are trapped. The maximum pollutant levels are recorded in the positions x = 0.200m and x = 0.300m.

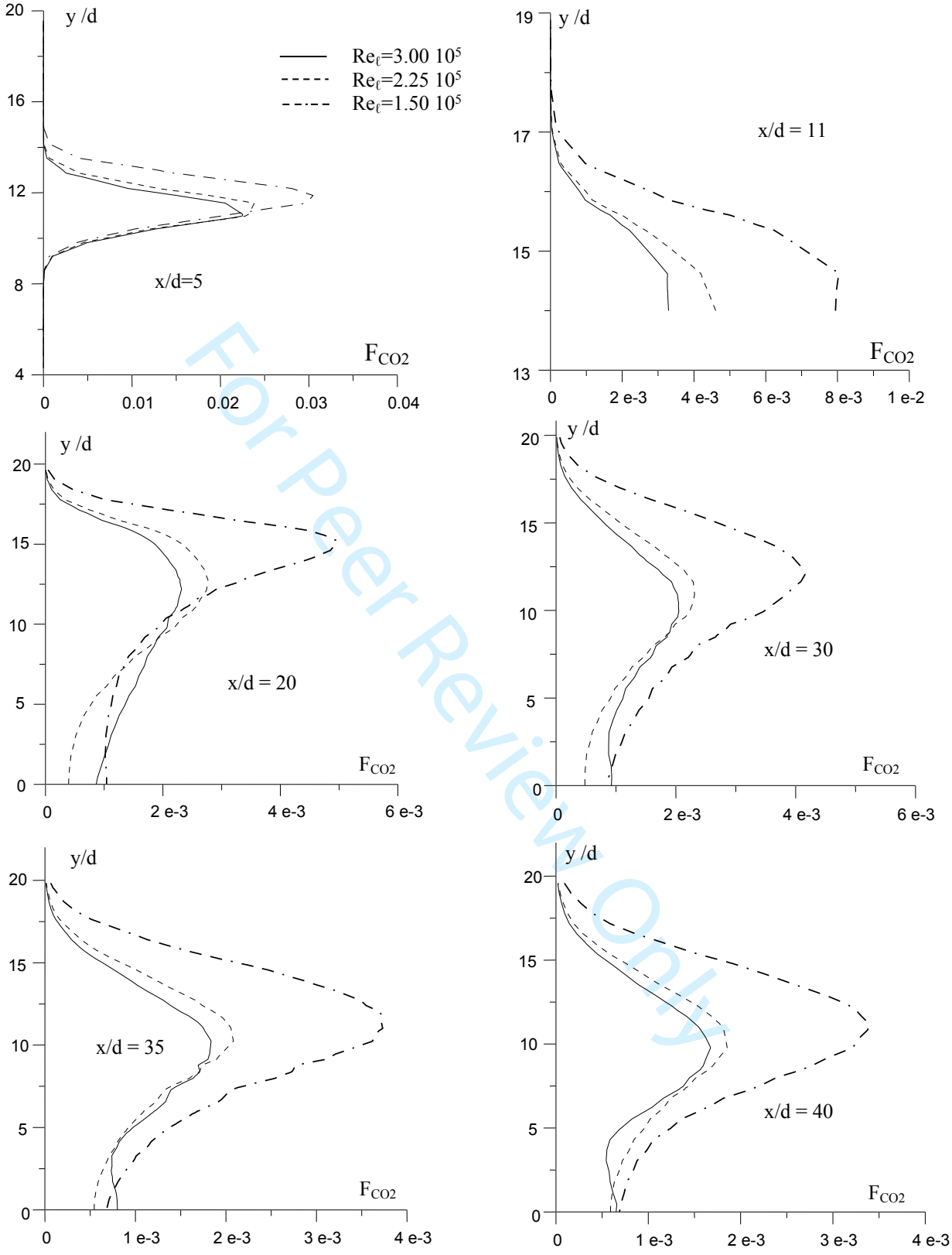

Figure 19. Evolution of carbon dioxide at different normal positions in the medium plane for Re=5000

Figure 20 presented the cross-sectional contours of the CO_2 mass fraction at different lateral planes (y) for the velocity ratio R=1.6 (Re=5000 and Re_t=9.4 10^4). It is evident that the pollutant ejected from the elevated jet was separated after hitting the upstream face of the cylindrical obstacle. The presence of the horseshoe vortex around the chimney was clearly shown in the two planes y/d=10 and y/d=10.5. However, in others planes, the horseshoe vortex was found around the obstacle. It was also observed that the presence of the counterclockwise-rotating bubble was behind the downstream face of the obstacle and it was well presented in the plane y/d=12.5. Over the plane y/d = 17, there was no pollutant.

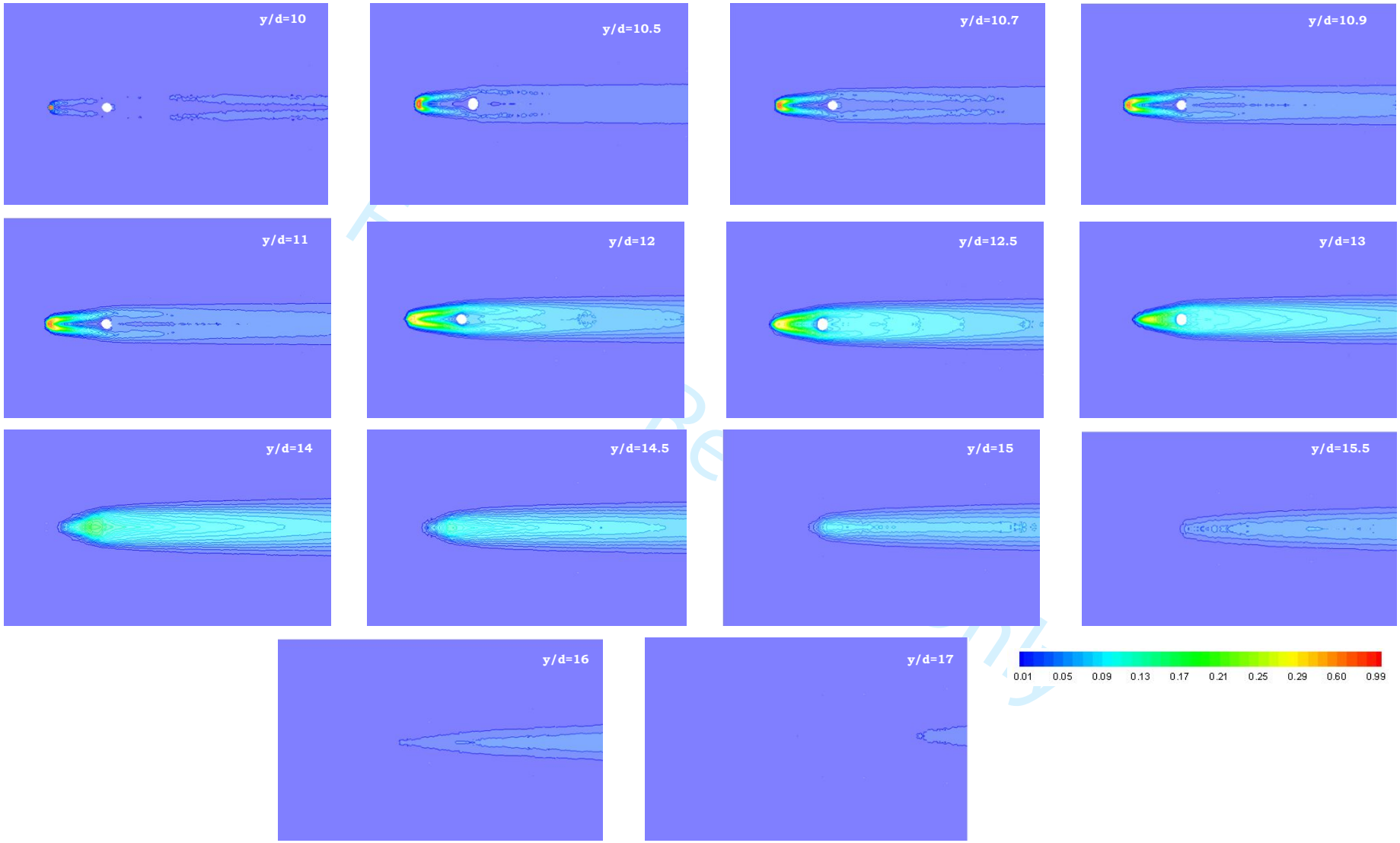

Figure 20. Cross-sectional contours of the CO_2 mass fraction at different lateral planes (y) for R=1.6 Re=5000 and Re_t=9.4 10^4

Figure 21 illustrated the cross-sectional contours of the CO_2 mass fraction around the cylindrical obstacle at various and successive normal planes (x) for the velocity ratio R=1.6 (Re=5000 and Re_ℓ=9.4 10^4). At the pollutant nozzle level, the ejection velocity is more important than the ambient velocity that can be noticed by the elevation of pollutant. The three phases of pollutant dispersion were clarly dedected. The pollutant flowing around a cylindrical topographic obstacle was obliged to be immobilized at the cylindrical obstacle surface accordingly to frictional coupling between the pollutant and the cylindrical obstacle boundary. The aspect of the flow promptly above the boundary depended on the impact of viscous effects, as determined by the velocity ratio and the Reynolds number. The pollutant is immediately above the surface of the cylindrical obstacle and then adopts the shape of a thin boundary layer on which the flow velocity rises from zero at the surface to approximately the ambient velocity u_∞ away from the surface. The boundary layer fluid percolating the obstacle surface at certain point confluenced an adverse pressure gradient. The boundary layer had a tendency to separate from the obstacle and shed its vorticity into the internal fluid. Boundary layer separation was the cause of wake generation in most flows of interest in engineering applications and problems. In the normal cross-section, the formation of the essential pair of vortices rotating in the wake directly behind the building was noticeble. The rotating pair was visualized in many normal planes upstream the chimney where there was no information about the pollutant only the air flow was viewed. Between the chimney and the cylindrical obstacle, the mass fraction contours showed the maximun fraction presented in this gap. In the third region, the size of the rotation pair become considerably bigger.

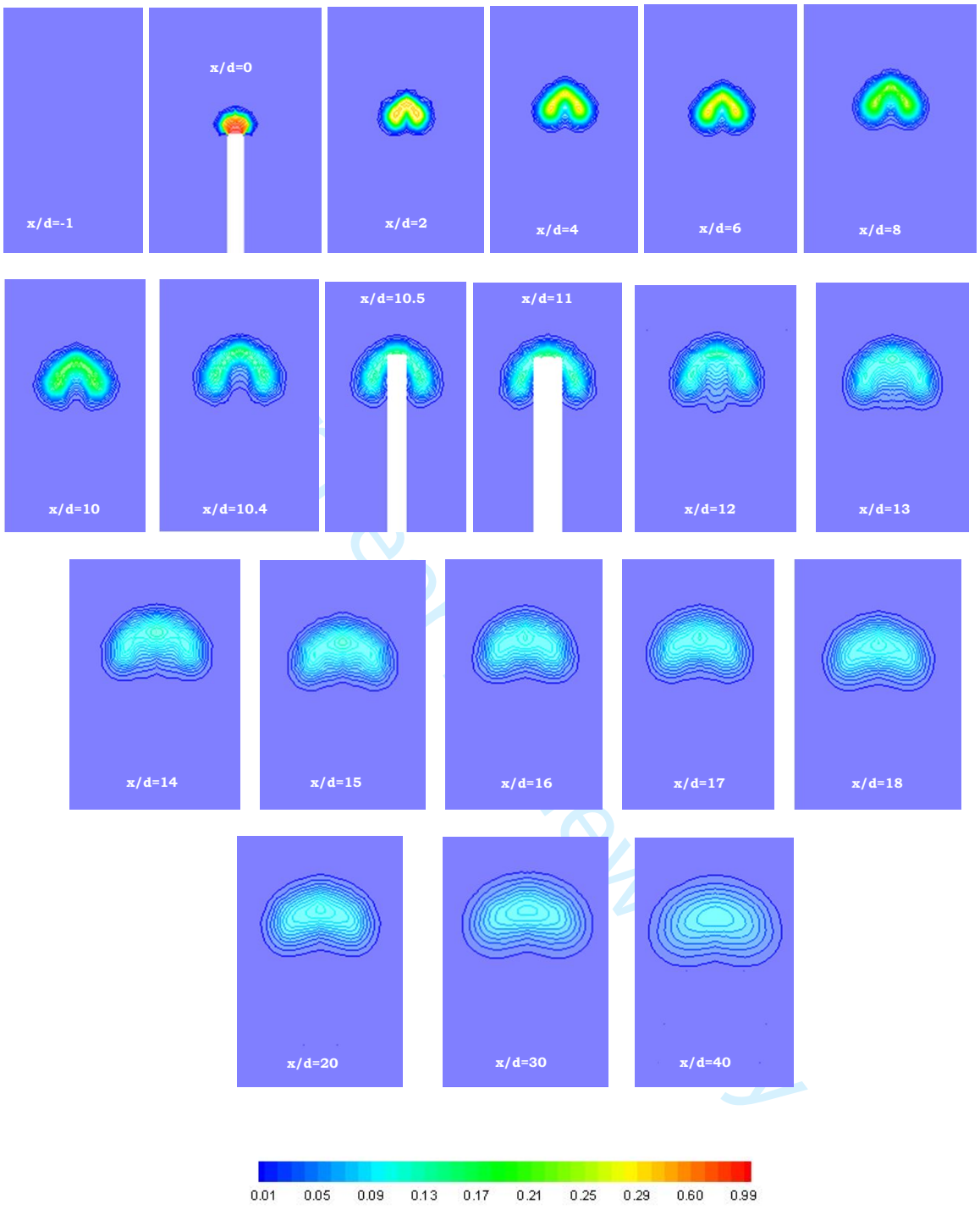

Figure 21. Cross-sectional contours of the CO_2 mass fraction around the cylindrical obstacle at different normal planes and for R=1.6

CONCLUSION

An experimental and numerical investigation of the evolution of chimney flow ejected into a crossflow ambient air flow stream with the presence of a cylindrical obstacle had been accomplished. The visualization of flow patterns of the plume from a stack in the vicinity of the obstacle had been examined. Contrary to most of the previous CFD studies of urban dispersion which focused on the far-field spread of pollutants, the present simulations focused on the region close to the chimney jet, the obstacle and in the surrounding. They were validated by comparison with wind-tunnel measurements for four different wind velocities, for which a high-rise obstacle is located immediately upstream of the emitting chimney. The agreement between numerical simulations using the second order turbulence model (RSM) and wind-tunnel measurements was good. The pollutant dispersion around the cylindrical obstacle was carried out for various cases of increasing wind velocity. It is found that the wind velocity has a pronounced influence on the flow structure. The flow characteristics including separation point, vortex – shedding behavior, pressure coefficient evolution and Strouhal number are studied. It is shown that the dispersion of low-velocity exhaust helps the formation of the recirculation bubble, in the roof zone. We determine dynamic, thermal and mass characteristics of these fields in many positions in and above the recirculation region. The results indicated that the pollutant mass fraction spread was high near the elevated jet and decreased with increasing distance from the elevated source. For a higher wind velocity, the flow motion and separation increased in the wake zone, and the pollutant mass fraction of the lateral spread at the average chimney height decreased. The vortex circulation flow was fast and strong, and the pollutant mass fraction of the vertical spread was low.

DECLARATION OF CONFLICTING INTERESTS

The author(s) declared no potential conflicts of interest with respect to the research, authorship, and/or publication of this article.

AUTHORS' CONTRIBUTION

"All authors contributed equally in the preparation of this manuscript."

ACKNOWLEDGMENT

The authors extend their appreciation to the Deanship of Scientific Research at King Khalid University, Saudi Arabia for funding this work through Large Groups (Project under grant number RGP.2/24/1443)

REFERENCES

1. Goyal P, Singh MP and Bandyopadhyay TK. Environmental studies of SO2, SPM and NOx over Agra with various methods of treating calms. Atmos Environ 1994; 28: 3113–3123.
2. Arya SP. Modeling and parameterization of near source diffusion in weak winds. J ApplMeteorol 1995; 34: 1112–1122.
3. Sharan M and Yadav A.K. Simulation of diffusion experiments under light wind, stable conditions by a variable K-theory model. Atmos Environ 1998; 32: 3481–3492.
4. Okamoto S and Shiozawa K. Validation of an air pollution model for the Keihin area. Atmos Environ 1978;12: 2139–2149.
5. Schofield W and Logan E. Turbulent Shear Flow Over Surface-Mounted Obstacles. ASME J Fluids Eng 1990; 112: 376–385.
6. Eckerle WA and Awad JK. Effect of Freestream Velocity on the Three-Dimensional Separated Flow Region in Front of a Cylinder. ASME J Fluids Eng 1991; 113: 37–44.
7. Martinuzzi R and Tropea C. The Flow Around Surface-Mounted, Prismatic Obstacles Placed in a Fully Developed Channel Flow. ASME J Fluids Eng 1993; 115: 85–92.
8. Higson HL, Griffiths RF, Jones CD, Hall DJ: Concentration measurements around an isolated building: a comparison between wind tunnel and field data: Atmos Environ 1994;11:1827–1836.
9. Sada K: Wind tunnel experiment of tracer gas diffusion within unstable boundary layer over coastal region: Atmos Environ 2002; 30: 4757–4766.
10. Marvoidis I, Griffiths RF and Hall DJ. Field and wind tunnel investigations of plume dispersion around single surface obstacles. Atmos Environ 2003; 37: 2903-2918.
11. Dutta S, Panigrahi PK and Muralidhar K. Effect of orientation on the wake of a square cylinder at low Reynolds numbers. Indian J Eng Mater Sci 2004; 11: 447-459.
12. Lin C, Ooka R, Kikumoto H, et al. Wind tunnel experiment on high-buoyancy gas dispersion around isolated cubic building. J Wind Eng Ind Aerodyn 2020; 202: 104226.
13. Abdel dayem AM and Bayomi NN. Experimental and numerical flow visualization of a single square cylinder. Int J Comput Methods Eng Sci Mech 2006; 7: 113-127.
14. Mahjoub Saïd N, Mhri H, Le Palec G, et al. Experimental and numerical analysis of pollutant dispersion from a chimney. Atmos Environ 2005; 39: 1727-1738.
15. Mahjoub Saïd N, Habli S, Mhri H, et al. Flow field measurement in crossflowing elevated jet. ASME J Fluids Eng 2007; 129: 551-562.
16. Mahjoub Saïd N, Mhri H, Bournot H and Le Palec G. Experimental and numerical modelling of the three-dimensional incompressible flow behaviour in the near wake of circular cylinders. J Wind Eng Ind Aerodyn 2008; 96: 471-502.
17. Lin C, Ooka R, Kikumoto H, et al. CFD simulations on high-buoyancy gas dispersion in the wake of an isolated cubic building using steady RANS model and LES. Build Environ 2021; 188: 107478.
18. Ma H, Zhou X, Tominaga Y, Gu M. CFD simulation of flow fields and pollutant dispersion around a cubic building considering the effect of plume buoyancies. Build Environ 2022; 208: 108640.
19. Jiang G and Yoshie R. Side ratio effects on flow and pollutant dispersion around an isolated high-rise building in a turbulent boundary layer. Build Environ 2020; 180: 107078.

20. Adair D. Numerical calculations of aerial dispersion from elevated sources. Appl Math Model 1990; 14: 459- 476.
21. Wang G and liang X. Development and evolution of flow over three dimensional cylinder. Chin Phys B 2005; 14: 1392-1397.
22. Huang YD, Hu XN and Zeng NB. Impact of wedge-shaped roofs on airflow and pollutant dispersion inside urban street canyons. Build Environ 2009; 44: 2335-2347.
23. Huang YD and Zhou ZH. A numerical study of airflow and pollutant dispersion inside an urban street canyon containing an elevated expressway. Environ Model Assess 2013; 18:105-114.
24. Huang YD, He WR and Kim CN. Impacts of shape and height of upstream roof on airflow and pollutant dispersion inside an urban street canyon. Environ Sci Pollut Res 2015; 22: 2117–2137.
25. Huang JM, Hsu SP, Wu YL, et al. The Effect of Ventilation Types on Pollutant Removal in a Large Space Plant with Multiple Pollutant source. Indoor Built Environ 2011;000;000:1–13
26. Abassi W, Aloui F, Laurent K, et al. Experimental and Numerical Investigations Using Lattice Boltzmann Method to Study Shedding Vortices in an Unsteady Confined Flow Around an Obstacle. ASME J Fluids Eng 2015; 137: 101203.
27. Korycki M, Łobocki L and Wyszogrodzki A. Numerical simulation of stratified flow around a tall building of a complex shape. Environ Fluid Mech 2016; 16:1143–1171.
28. Keshavarzian E, Ruizhi J, Kejun D, et al. Effect of pollutant source location on air pollutant dispersion around a high-rise building. Appl Math Model 2020; 81: 582–602.
29. Gomit G, Beaulieu C, Braud P and David L. Démarche d'estimation des incertitudes en PIV basée sur la méthode GUM. 16th Francophone Congress of Laser Techniques (CFTL), Dourdan, France, 2018.
30. Sciacchitano A. Uncertainty quantification in particle image velocimetry. Meas Sci Technol 2019; 30: 092001.
31. International Organization for Standardization ISO 2018, Guide to the expression of Uncertainly in Measurement (International Organization for Standardization).
32. Wieneke B. PIV uncertainty quantification from correlation statistics. Meas Sci Technol 2015; 26: 074002.
33. Boomsma A, Bhattacharya S, Troolin D, Pothos S and Vlachos P. A comparative experimental evaluation of uncertainty estimation methods for two-component PIV. Meas Sci Technol 2016; 27: 094006.
34. Westerweel J. Theoretical analysis of the measurement precision in particle image velocimetry. Exp Fluids 2000; 29: S3–S12.
35. Mahjoub Said N, Mhri H, Golli S, et al. Three dimensional numerical calculations of a jet in an external crossflow: application to pollutant dispersion. ASME J Heat Transfer 2003; 125: 510-522.
36. Demuren AO and Rodi W. Three Dimensional Numerical Calculations of Flow and Plume Spreading Past Cooling Towers. ASME J Heat Transfer 1987; 109: 113–119, 1987.
37. Mi, J., Nobes, D. S., and Nathan, G. J., (2001), Influence of Jet Exit Conditions on the Passive Scalar Field of an Axisymmetric Free Jet," J. Fluid Mech., 432, pp. 91–125.
38. Patankar SV and Spalding DB. A calculation procedure for heat, mass and momentum transfer in three-dimensional parabolic flows. Int J Heat Mass Transfer 1972; 15: 1787–1806.
39. Roshko, A. 1954 On the drag and shedding frequency of bluff cylinders. Nut. Adv. Comm. Aero., Wash., Tech. Note 3169.

40. Roshko, A. 1955 On the wake and drag of bluff bodies. J. Aero. Sci. 22, 124-32.
41. Ribner, H. S. & Etkin, B. 1958 Noise research in Canada. Proc. 1st Int. Congr. Aero. Sci., Madrid (publ. by Pergamon Press, London, 1959).

Figure Captions List

Figure 1 Chimney and obstacle positions in the wind tunnel

Figure 2 Mainstream velocity 20 diameters downstream of the inlet test cross section.

Figure 3 Different types of vortical structure associated with the chimney -jet near field in a horizontal plane y/d=1.1, without cylindrical obstacle

Figure 4 Cross-sectional instantaneous vorticities of the flow downstream chimney-jet and their wakes, Re=1875 and Re_ℓ=1.87 10^4

Figure 5 (a) Mean velocity field, (b) instantaneous longitudinal-velocity, (c) mean vorticity field, (d) instantaneous vorticity, Re=1875 and Re_ℓ=1.87 10^4

Figure 6 Mesh sensitivity analysis

Figure 7 Effect of the wind velocity on turbulent structures

Figure 8 Effect of the obstacle presence on the plume evolution, Re=5000

Figure 9 Contours of a) mean velocity, b) vertical velocity component $\tilde{w}$ and c) longitudinal velocity component $\tilde{u}$vectors (Re=5000 and Re_ℓ = 3 10^5)

Figure 10 Influence of wind 8velocity on the evolution of the plume emerging from the chimney around a cylindrical obstacle, Re=5000

Figure 11 Velocity vectors for various velocity ratios in the presence of a cylindrical obstacle

Figure 12 Mean longitudinal $\tilde{u}$ velocity profiles at R=1

Figure 13 Mean normal $\tilde{v}$ velocity profiles at R=1

Figure 14 Horizontal and vertical Reynolds stress at different streamwise locations

Figure 15 Mean velocity contours of the global chimney jet' progression around the cylindrical obstacle at different lateral planes and under different wind velocities and Re = 5 10^3

Figure 16 Strouhal vs. Reynolds number for the chimney (a) and the obstacle (b)

Figure 17 Pressure coefficients on the center plane (z=0): (a) windward facade; (b) leeward facade.

Figure 18 Temperature evolution around the cylindrical obstacle at different lateral planes for Re=5000 and Re_ℓ =3 10^5

Figure 19 Evolution of carbon dioxide at different normal positions in the medium plane for Re=5000

Figure 20 Cross-sectional contours of the CO_2 mass fraction at different lateral planes (y) for R=1.6, Re=5000 and Re_ℓ=9.4 10^4

Figure 21 Cross-sectional contours of the CO_2 mass fraction around the cylindrical obstacle at different normal planes and for R=1.6

Table Caption List